Chapter 4

Heat Withdrawal in Continuous Casting of Steel

Klaus J. Schwerdtfeger, Professor, Technical Institute Clausthal

4.1 Introduction

Fig. 4.1 shows the different cooling sites of a continuous casting machine. In the copper mold (a) heat is transported to the cooling water. A shell solidifies, attaining a thickness of 1 to 3 cm at the end of the mold. The interior of the strand stays liquid or mushy for many meters downward, depending on the casting rate and the strand thickness. Below the mold, in the so-called secondary cooling zone, cooling is performed by water sprays (b), by contact with water cooled support (and driven) rolls (c), and in the lower part of the machine, beyond the spray zone, mainly by radiation (d) and contact with the rolls.

Two principal methods are used to investigate the heat transfer in continuous casting. The main way is to measure cooling water temperatures, mold wall temperatures, strand temperatures and

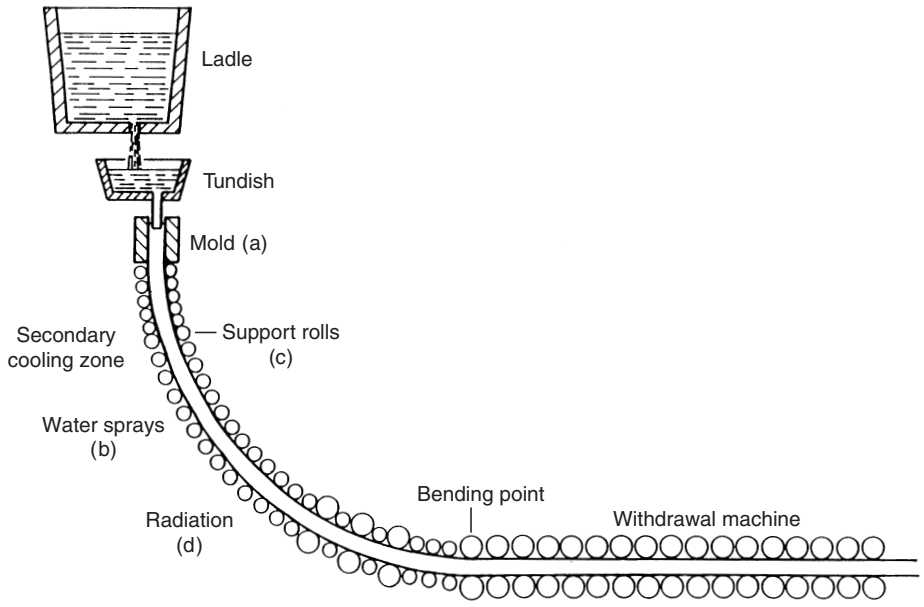

Fig. 5.1 Different zones of heat transfer in a continuous casting machine.

shell profiles in the actual operation, and then deduce from these data heat flux densities and/or heat transfer coefficients. The other way is to investigate the unit heat transfer operations theoretically or experimentally in the laboratory, viz. heat transfer through layers of casting flux or heat transfer under spray nozzles. In the following sections the various heat withdrawal phenomena in continuous casting will be discussed.

4.2 Heat Withdrawal in the Mold

Continuous casting molds are made of copper alloys and are internally cooled with water. The active cooling length of molds for continuous casting of steels ranges from 600 to 900 mm. To decrease the friction between mold and strand, a lubrication medium is added to the mold, which is casting flux made of mineral materials for slab and bloom casting, or oil for small section billet casting. The lubricant forms a layer between the strand and mold wall. Farther down, the solid shell may shrink away from the mold because of thermal contraction. A gap is formed that is filled with gas. Obviously, the mechanism of heat transfer from the surface of the strand to the cooling water is complex, involving resistances in the layer of flux, in a gap filled with gas, in the copper wall and in the water.

From the comparison of thermal conductivities in Table 4.1, it can already be assumed that most of the thermal resistance of the mold is in the gas gap.

Table 4.1 Comparison of Thermal Conductivities of Materials Present in a Continuous Casting Mold

	Temperature (°C)	Thermal conductivity ($W\ m^{-1}\ K^{-1}$)
Steel St 37	1200	29
Copper	30–130	385
Casting flux (λ_{app})	1000–1300	0.5 to 1.2
Water	25	0.62
Nitrogen	1000	0.075
Radiation conductivity	1400 (T_0)	0.075
of gas gap at d_{gap} = 1 mm	1000 (T_0)	0.043

4.2.1 Heat Flow Through a Layer of Casting Flux

Fig. 4.2 shows schematically the casting flux layer in the upper region of the mold where a macroscopic gas gap does not yet exist, and the temperature profile between the steel shell and the mold wall. The flux, which has a liquidus temperature around 1150°C, is liquid in contact with the hot strand and solid at the mold. There may be a mushy zone between the liquid and the solid parts consisting of a crystal-melt mixture. Whereas perfect contact can be assumed between the strand surface and the liquid, this is not necessarily the case between the solid and the mold. That is, depending on the composition of the flux, its cold surface at the wall of the mold may not be smooth. The wrinkles are filled with gas. So, also in the upper part of the mold where no macroscopic gap exists, there can be an effective microscopic gap causing an interface resistance at the mold wall. The transport of heat through the layer is both by conduction and radiation. The latter is complicated, particularly also because the solid region of the layer may be partially in the glassy state and partially crystalline.

A theoretical modeling of the radiative and conductive heat transfer through a layer consisting of sublayers of different phases is rather difficult, although this has been attempted in recent literature.[1] For the engineering application it suffices to have the experimental data for the overall heat flux that can be obtained in the laboratory with apparati designed for this purpose. For instance, the strand

can be simulated by a steel plate that is heated by an electric current.[2,3] The plate has a trough in which the casting flux is fused. A copper block, cooled internally with water, serves as the mold. The setup is instrumented with thermocouples for determination of the heat flux (via temperature gradient in the copper) and of the mold and strand-side temperatures T_m and T_0, respectively. Fig. 4.3 shows heat flux densities obtained in such a manner with two different casting powders. Fig. 4.4 gives apparent layer conductivities λ_{app} deduced on the basis of equation:

$$q = \frac{\lambda_{app}}{d_{cf}}(T_0 - T_m) \qquad \text{(Eq. 4.1)}$$

The apparent thermal conductivity λ_{app} increases with strand temperature T_0, indicating the effect of radiation. There is also a marked influence of composition (compare Figs. 4.4a and b), which is caused by the different absorption coefficients of the oxides, and by the effects of the different oxides on making the layer partially crystalline and on producing a non-smooth interface at the mold side. Although the actual measurements (Fig. 4.3) were taken with somewhat thicker flux layers than usually present in continuous casting and partially (flux 1) do not extend to 1500°C, the λ_{app} values (Fig. 4.4) can readily serve to compute the heat flux density also for smaller layer thickness and higher temperature.

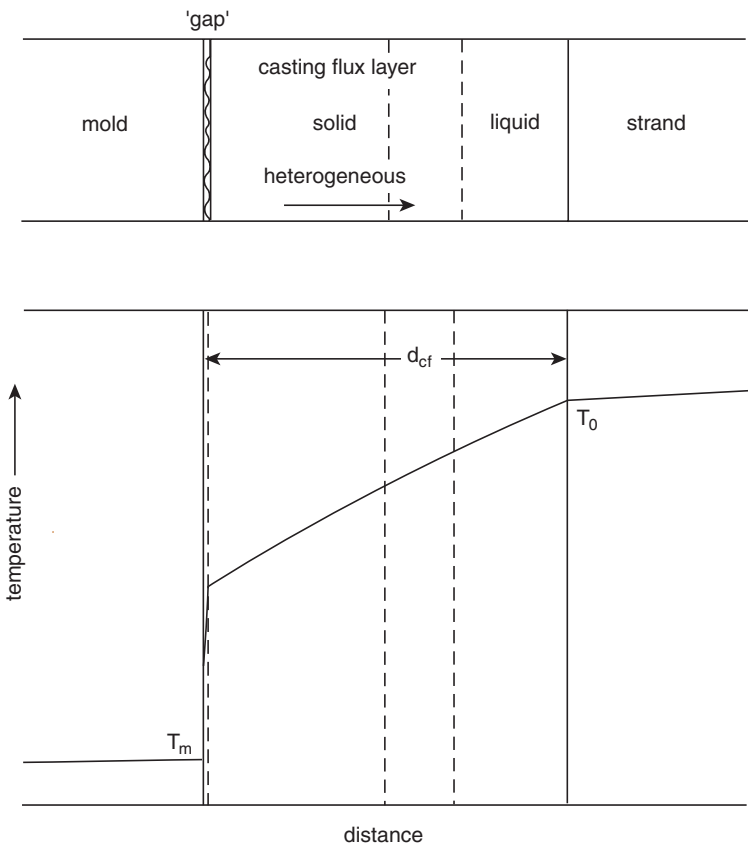

Fig. 4.2 Schematic representation of casting flux layer between the surface of the strand and the wall of the mold, and temperature profile. Upper region of the mold.

4.2.2 Heat Flow Through a Gas Gap

When the temperature along the strand surface drops below the solidus temperature of the casting flux, the flux layer becomes completely solid. Due to the shearing forces caused by the relative motion between the strand and mold and due to shrinkage of the flux, the coherence of the layer may be destroyed, and there will be, at least locally, heat exchange between the strand surface and the mold wall directly over a gas gap. Also, if in the lower part of the mold the conicity of the mold does not balance the shrinkage of the strand shell or if the ferrostatic pressure does not suffice to press the strand shell against the mold, a macroscopic gap will develop. The gas in the gap is formed mainly from air (penetrating into the gap from the lower end of the mold) and consists primarily of nitrogen, since most of the oxygen has been removed from the air by reaction with the strand surface. It may contain some water vapor from the water sprays below the mold and, in the upper part of the mold, hydrogen generated by reduction of water by the steel surface. It may also contain some carbon dioxide and monoxide originating from various reactions between the gas, the steel and the flux.

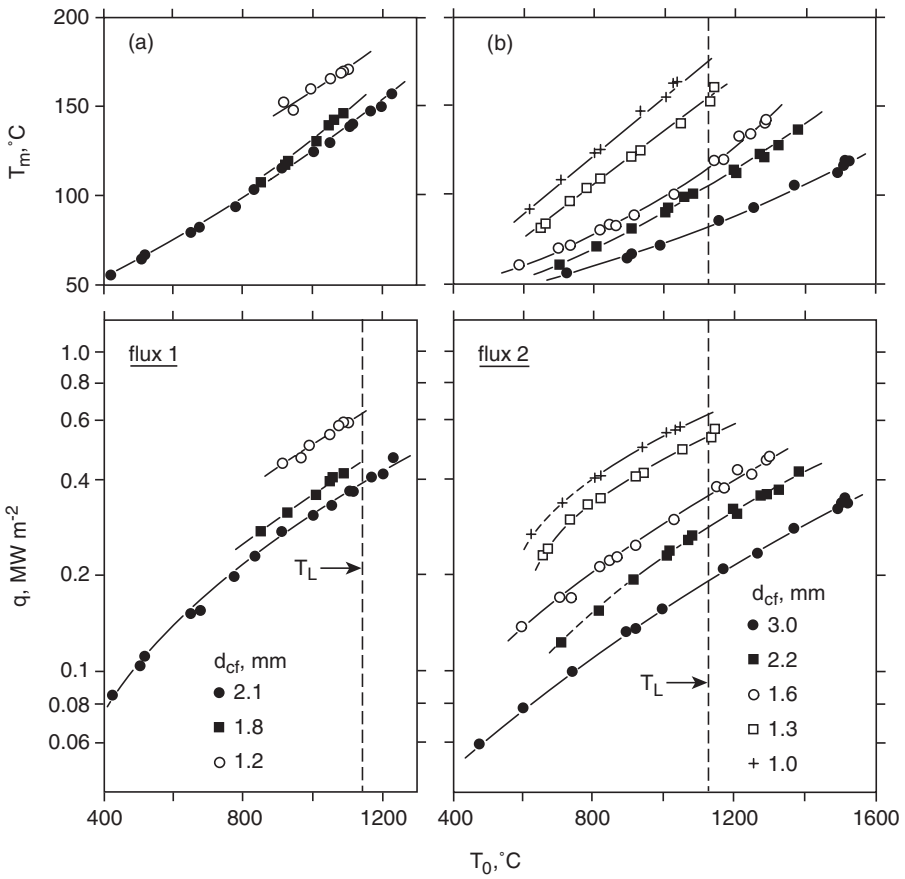

Fig. 4.3 Laboratory data on heat transfer through layers of casting flux: (a) flux 1 (32% SiO_2, 32% CaO, 7.5% Al_2O_3, 4.5% Na_2O, 1.1% Fe, 4.5% F, 0.6% MgO, 0.2% TiO_2, 0.3% MnO, 1.0% K_2O, 9% C_{tot} in the powder state; C was removed prior to the experiment by preheating in air; (b) flux 2 same as flux 1, but with 3.5% FeO added. *From Ref. 2.*

The heat transfer over a gas gap contained between two parallel metal plates has been investigated with the same setup as described in Section 4.2.1.[2,4] In Fig. 4.5a the obtained heat flux densities are plotted against the hot surface temperature T_0 (strand temperature). The cold surface temperature T_m (mold temperature) is given in Fig. 4.5b. Since the optical thickness of a thin gas layer is small, the total heat flux can be written as the sum of conductive and radiative components:

$$q = q_c + q_r \qquad \text{(Eq. 4.2)}$$

which are independent of each other and are given as:

$$q_c = \lambda_{gas} \frac{\partial T}{\partial x} \qquad \text{(Eq. 4.3)}$$

$$q_r = \frac{\sigma(T_0^4 - T_m^4)}{\varepsilon_0^{-1} + \varepsilon_m^{-1} - 1} \qquad \text{(Eq. 4.4)}$$

The radiation constant σ has the value 5.669×10^{-8} W m^{-2} K^{-4}. Using the expression

$$\lambda_{95N_2-5H_2} = 3.565 \times 10^{-4}\, T^{0.768}, \text{ W m}^{-1}\text{ K}^{-1} \qquad \text{(Eq. 4.5)}$$

for the 95% N_2–5% H_2 layer applied in the experiments of Fig. 4.5, equation 4.3 can be integrated:

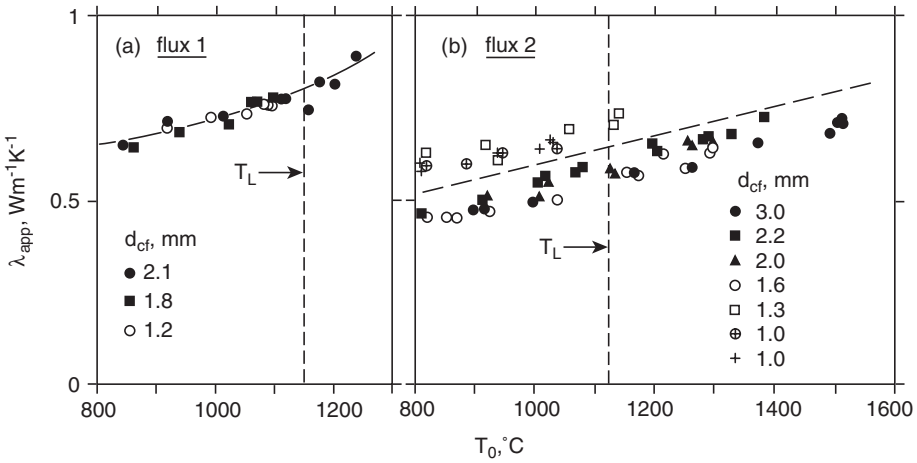

Fig. 4.4 Apparent layer thermal conductivities as a function of strand temperature: (a) flux 1; (b) flux 2. *From Ref. 2.*

$$\int_0^{d_{gap}} q_c \, dx = q_c \, d_{gap} = \int_{T_m}^{T_0} \lambda(T) dT \qquad \text{(Eq. 4.6)}$$

yielding

$$q_c = \frac{2.016 \times 10^{-4} (T_0^{1.768} - T_m^{1.768})}{d_{gap}}, \ Wm^{-2} \qquad \text{(Eq. 4.7)}$$

with all temperatures in K and d_{gap} in m.

Hence, the total heat flux density is given by:

$$q = \frac{2.016 \times 10^{-4} (T_0^{1.768} - T_m^{1.768})}{d_{gap}} + \frac{\sigma (T_0^4 - T_m^4)}{\varepsilon_0^{-1} + \varepsilon_m^{-1} - 1}, \ W \ m^{-2} \qquad \text{(Eq. 4.8)}$$

Equation 4.8 is perfectly fulfilled by the measurements yielding an average emissivity, defined as $\varepsilon_{0+m}^{-1} = 0.5 \ (\varepsilon_0^{-1} + \varepsilon_m^{-1})$, of the copper and steel surfaces of $\varepsilon_{0+m} = 0.4$. This value refers to the metallic surfaces (in reducing gas) in the laboratory setup. For oxidized surfaces ε_{0+m} is larger.

By comparing the data in Fig. 4.5 with those in Fig. 4.3, it is evident that the heat flux through a nitrogen (plus hydrogen) gap is low compared to that through a casting flux layer. Gap formation causes a high resistance to the heat transfer between strand and mold and decreases the cooling capacity of the continuous casting mold.

4.2.3 Heat Flow Through a Water-Cooled Copper Plate and Total Resistance for Heat Transfer in the Mold

The heat transfer in the copper wall from the hot side to the water-cooled cold side involves resistances in the copper body and at the boundary between the copper and the water. In the mold there should be no boiling; that is, the heat flow occurs in the stability domain of water. However, there can be steam formation if the water flow rate is too low, causing distortion of the mold and deleterious effects on the strand. Evaporation plays an important role, however, in the spray cooling of the secondary cooling zone. We will first discuss some fundamental aspects of heat transfer into water at a heated plate.

4.2.3.1 General Characteristics of Heat Transfer from a Heated Wall into Water

The mechanism of heat transfer from a heated plate into water depends strongly on temperature, as has been known for a long time from studies of the cooling of hot bodies in stagnant (pool boiling cooling) and streaming water (flow boiling cooling) or from heat transfer in pipes. Fig. 4.6 shows a diagram in which the heat flux density is plotted against the difference $T_n - T_w$ between the wall temperature T_n and the bulk temperature T_w (= 40°C) of the water. Several regions have to be distinguished:

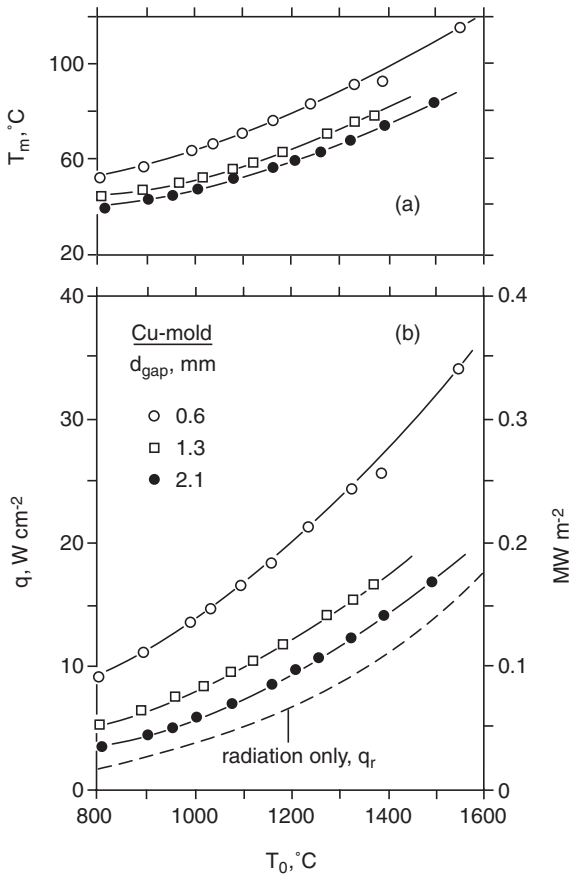

Fig. 4.5 Heat transfer through a gap filled with nitrogen-hydrogen gas.

- At low temperature (small temperature difference $T_n - T_w$) there is little or no evaporation. The small bubbles formed at the surface are detached and recondense in the cold bulk of the water. The heat transfer coefficient can be explained quite well by the laws for convective transport at a heated wall.
- If the surface temperature exceeds the boiling point by a certain value, there is a region of so-called nucleate boiling. The formation of steam bubbles occurs at the wall, with the number of nucleation sites increasing with temperature. The detaching bubbles cause a vigorous stirring of the water close to the wall, which leads to a strong increase of heat transfer.
- At a certain temperature the heat transfer coefficient reaches a maximum at the so-called burn-out point. The following decrease is brought about by the formation of an isolating steam film between the surface and the bulk of the water. This film is not yet stable. The temperature range is called that of unstable film boiling.
- Finally, the steam film becomes stable at the Leidenfrost temperature (about 250°C in Fig. 4.6), completely preventing the contact of the water with the hot surface. Above this temperature is the range of stable film boiling, in which the heat flux density again increases with increasing temperature.

4.2.3.2 Heat Transfer to Cooling Water in Continuous Casting Molds

The heat flow in the copper wall of a simple tube mold for billet casting is essentially one-dimensional, except at the edges of rectangular molds and in the meniscus region, but it is two-dimensional around the water ducts of a slab mold. Correlations for the heat transfer coefficient, which take into account the specific features of a continuous casting mold, are not available. However, approximate values can be deduced from the correlations for the Nusselt number for flow in pipes.

The schematics of the temperature profile between the strand temperature T_0 and the water temperature T_w and of the geometry are depicted in Figs. 4.7 and 4.8. For the billet mold, Fig. 4.7a, the heat flux densities in the thermal boundary layer of the water and in the copper wall are expressed as:

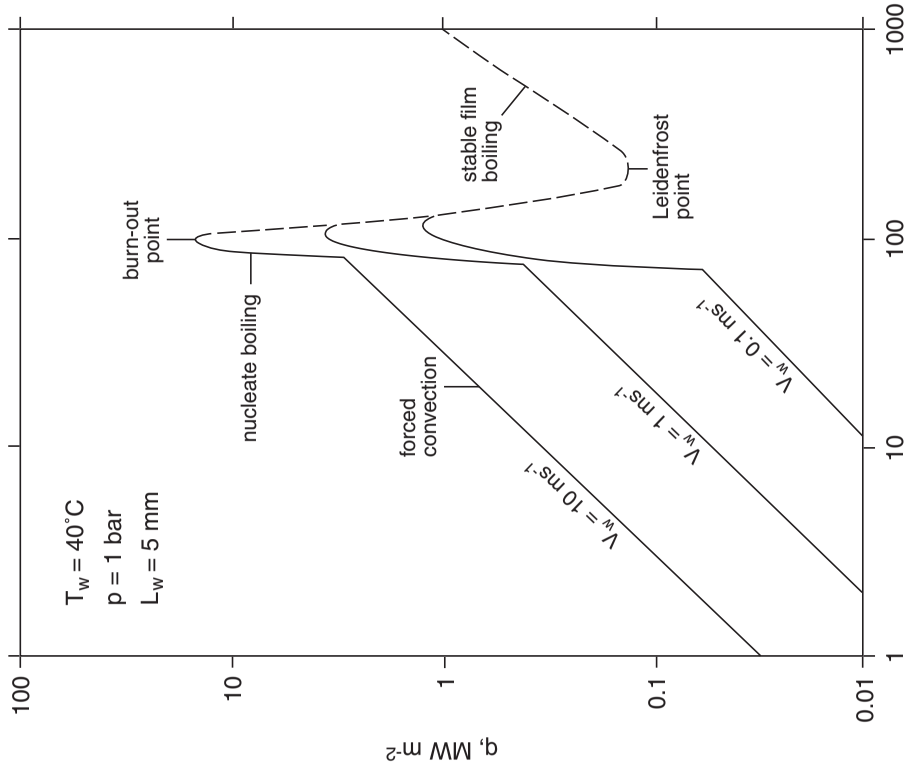

Fig. 4.6 Thermal transfer regimes at the copper/water interface in a continuous casting mold. *From Ref. 5.*

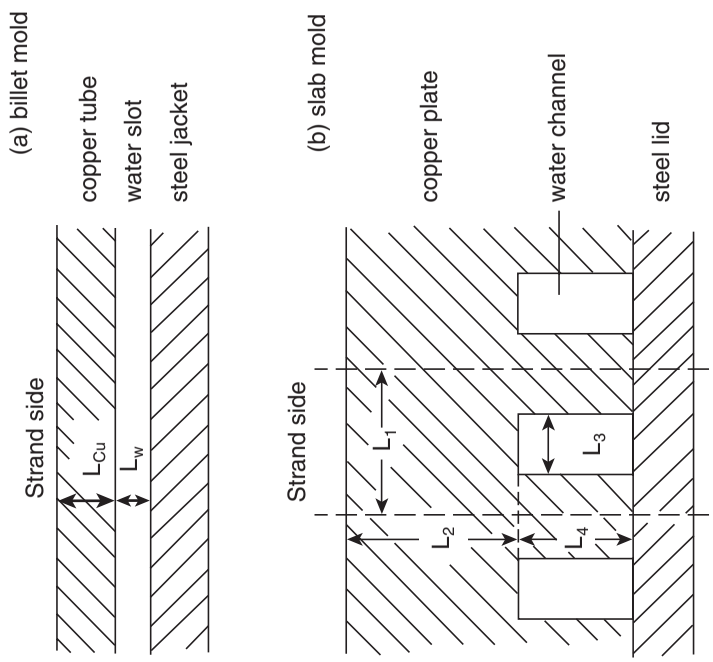

Fig. 4.7 Water duct in continuous casting molds: (a) billet mold (tube mold); (b) slab mold.

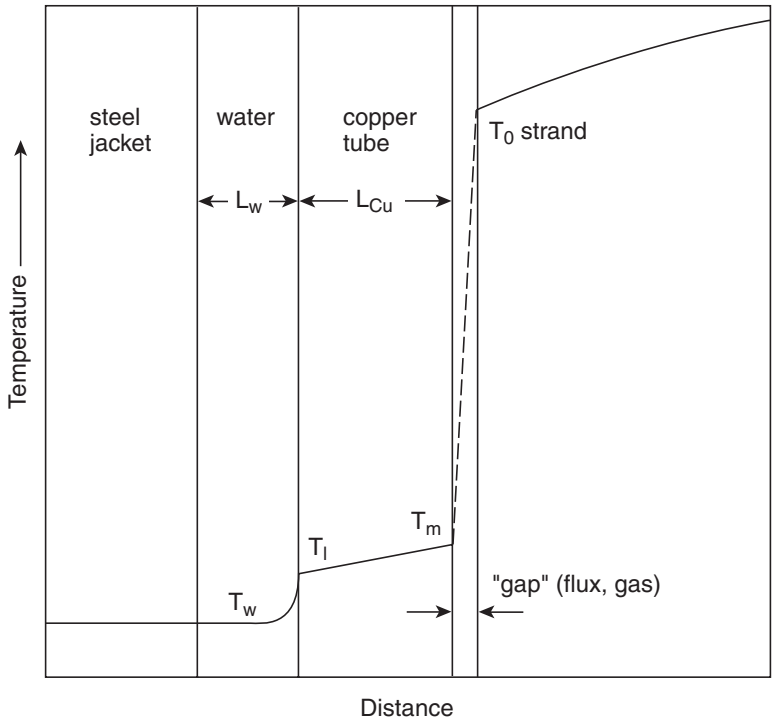

Fig. 4.8 Temperature evolution between surface of the strand and cooling water of the mold.

$$q = h_w\ (\text{billet mold})\,(T_l - T_w) = \frac{\lambda_{Cu}}{L_{Cu}}(T_m - T) \qquad \text{(Eq. 4.9)}$$

In the slab mold, Fig. 4.7b, the contact areas of the copper body with the strand and with the water are different. Hence, the heat flux densities are different at both sides. Also, the conduction path in the copper varies between L_2 and $L_2 + L_4$. The first effect can be taken into account by using the equality $q\ L_1 = q_w\ L_{D,eff}$, where q_w is an average heat flux density at the sides of the water duct and $L_{D,eff}$ is an effective periphery of the water duct. The second can be accounted for by application of an effective copper thickness, $L_{Cu,eff}$.

Hence, for the slab mold

$$q = \left(\frac{L_{D,eff}}{L_1}\right) h_w\ (\text{slab mold})\,(T_l - T_w) = \frac{\lambda_{Cu}}{L_{Cu,eff}}(T_m - T_l) \qquad \text{(Eq. 4.10)}$$

Here, T_l is an average wall temperature. The values of $L_{D,eff}$ and $L_{Cu,eff}$ may be represented by various approximate formulae. Convenient expressions have been found to be:

$$L_{D,eff} = L_3 + 2L_4\left(1 - \frac{L_3}{L_1}\right) \qquad \text{(Eq. 4.11a)}$$

and

$$L_{Cu,eff} = L_2 + \frac{L_4}{2}\left(1 - \frac{L_3}{L_1}\right) \qquad \text{(Eq. 4.11b)}$$

The literature contains many forms of the correlation for the heat transfer coefficient in pipes.[6,7] The following is based on the equation:[6]

$$Nu = \frac{h_w D}{\lambda} = 0.026\,Re^{0.8}\,Pr^{1/3}\left(\frac{\eta}{\eta_l}\right)^{0.14} \qquad \text{(Eq. 4.12)}$$

with $Re = D\, v_w\, \rho/\eta$ and $Pr = c_p\, \eta/\lambda$, which is valid in the highly turbulent region (Re > 20,000). The material property factor $\lambda\, \rho^{0.8}\, Pr^{1/3}\, \eta^{-0.8}$ of water has been evaluated from the compiled data of λ, η, Pr and ρ and found to be close to linear with temperatures in the range of 10 to 60°C.[8,9] Hence, the expression for the heat transfer coefficient to water in a round pipe is:

$$h_w(\text{pipe}) = (1430 + 23T_w)\, v_w^{0.8}\, D^{-0.2} \left(\frac{\eta}{\eta_l}\right)^{0.14}, \text{ W m}^{-2}\text{ K}^{-1} \qquad \text{(Eq. 4.13)}$$

in which the water temperature T_w is in °C, the water velocity v_w in m s^{-1} and the pipe diameter D in m. The factor η/η_l between the viscosities of the water in the bulk stream η and at the hot wall η_l increases considerably with increasing temperature T_l at the wall, but due to the exponent 0.14 the effect of the viscosity ratio is still moderate. For instance, $(\eta/\eta_l)^{0.14}$ is 1.284 for T_w = 30°C and T_l = 200°C. Hence, the factor may be used if desired in the following application to continuous casting, but it may also be omitted in view of the other approximations. In application to the continuous casting molds, the diameter D is replaced by the hydraulic diameter D_{hydr} of the water duct in the mold:

$$D_{hydr} = \frac{4 \times \text{cross-section available for flow}}{\text{wetted perimeter}} \qquad \text{(Eq. 4.14)}$$

Hence, for the slot of width L_w of a billet mold (Fig. 4.7a)

$$D_{hydr} = 2L_w \qquad \text{(Eq. 4.15)}$$

and for the channels of a slab mold (Fig. 4.7b)

$$D_{hydr} = \frac{2L_3\, L_4}{L_3 + L_4} \qquad \text{(Eq. 4.16)}$$

Inserting equation 4.15 or 4.16 into equation 4.13 yields

$$h_w(\text{billet mold}) = (1245 + 20T_w)\, v_w^{0.8}\, L_w^{-0.2}, \text{ W m}^{-2}\text{ K}^{-1} \qquad \text{(Eq. 4.17)}$$

$$h_w(\text{slab mold}) = (1245 + 20T_w)\, v_w^{0.8} \left(\frac{L_3\, L_4}{L_3 + L_4}\right)^{-0.2} \qquad \text{(Eq. 4.18)}$$

with T_w in °C, v_w in m s^{-1} and the dimensions L in m. These equations are valid as long as there is no steam evolution in the duct. It is very important that the burn-out point is not approached in mold cooling (see Fig. 4.6). To ensure that such an event cannot occur, the flow velocity of the cooling water must be chosen so high that T_l is safely below the boiling point. Typical flow velocities are in the range of 5 to 10 m s^{-1}.

The total heat transfer coefficient between the strand surface and the cooling water of the mold, defined by:

$$q = h\,(T_0 - T_w) \qquad \text{(Eq. 4.19)}$$

is obtained from equations 4.1 and 4.9 or equations 4.1 and 4.10 as:

$$\frac{1}{h(\text{billet mold})} = \frac{1}{h_w(\text{billet mold})} + \frac{L_{Cu}}{\lambda_{Cu}} + \frac{d_{cf}}{\lambda_{app}} \qquad \text{(Eq. 4.20)}$$

$$\frac{1}{h(\text{slab mold})} = \left(\frac{L_1}{L_{D,eff}}\right)\frac{1}{h_w(\text{slab mold})} + \frac{L_{Cu,eff}}{\lambda_{Cu}} + \frac{d_{cf}}{\lambda_{app}} \qquad \text{(Eq. 4.21)}$$

Equations 4.20 and 4.21 can be rewritten in terms of resistances as:

$$R = R_w + R_m + R_{cf} \qquad \text{(Eq. 4.22)}$$

with:

$$R = \frac{T_0 - T_w}{q} = \frac{1}{h} \qquad \text{(Eq. 4.23)}$$

$$R_w = \frac{T_l - T_w}{q} = \frac{1}{h_w} \quad \left[\text{or} = \left(\frac{L_1}{L_{D,eff}}\right)\frac{1}{h_w}\right] \qquad \text{(Eq. 4.24)}$$

$$R_m = \frac{T_m - T_l}{q} = \frac{L_{Cu}}{\lambda_{Cu}} \quad \left[\text{or} = \left(\frac{L_{Cu,eff}}{\lambda_{Cu}}\right)\right] \qquad \text{(Eq. 4.25)}$$

$$R_{cf} = \frac{T_0 - T_m}{q} = \frac{d_{cf}}{\lambda_{app}} \qquad \text{(Eq. 4.26)}$$

If there is a gas gap instead of the casting flux layer (lower region of the mold), R_{cf} in equation 4.22 is replaced by:

$$R_{gap} = \frac{T_0 - T_m}{q} \qquad \text{(Eq. 4.27)}$$

R_{gap} can be taken from the experimental data (Fig. 4.5) or be computed with equation 4.8. Table 4.2 gives the typical numerical values for the different *R*s. It is evident that by far the main part of the total resistance is in the flux layer or in the gas gap. There the temperature drop is largest, as has already been indicated qualitatively in Fig. 4.8. The resistance of a gas gap is much larger than that of the casting flux layer. The cooling capacity of continuous casting molds is decreased strongly by the formation of gas gaps.

Table 4.2 Typical Magnitude of Heat Flow Resistances of the Different Regions Between the Strand Surface and the Cooling Water in a Continuous Casting Mold

Regime and physical data	R, m^2 K W^{-1}
boundary layer of water, L_w = 1 cm, v_w = 8 m s^{-1}, T_w = 25°C	4.3×10^{-5}
copper plate, L_{Cu} = 1 cm, λ_{Cu} = 385 W m^{-1} K^{-1}	2.6×10^{-5}
casting flux layer, d_{cf} = 0.5 mm, λ_{app} = 1 W m^{-1} K^{-1}	50×10^{-5}
gas gap, d_{gap} = 0.5 mm, 1200°C	420×10^{-5}

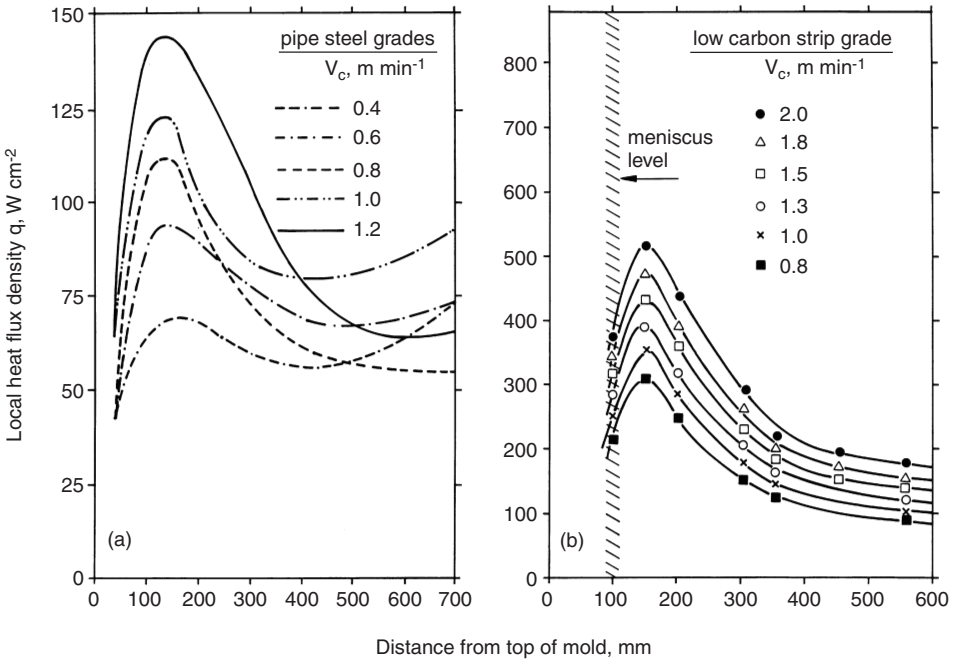

Fig. 4.9 Examples for heat flux distribution along the length of the mold: (a) bloom caster with steel mold *(from Ref. 11);* (b) slab caster *(from Ref. 12).*

Remember that equations 4.10, 4.11a, 4.11b and 4.21 for the slab mold represent approximations. The accurate treatment of the heat flow in the slab mold involves the computation of the two-dimensional temperature field in the cross-section of the copper body.

4.2.4 Plant Data on Mold Heat Transfer

The data on the unit heat transfer operations give insight into the different mechanisms operating in the mold, and they are useful tools in optimization efforts. However, the heat flux existing in reality must be measured on a live continuous casting mold. Such measurements are performed by determination of the temperature gradients in the copper plate of the mold using molds instrumented with thermocouples, and by determination of the increase of the temperature of the cooling water. The main parameter influencing the heat withdrawal in the mold is the casting velocity, but there are several other factors: the taper of the mold, the type of the mold (e.g., straight, curved), the guidance system below the mold, the type of the lubricant, the composition of the steel (e.g., carbon content) and the superheat. If the data are to be used in modeling work, it is useful to present them in the form of analytical expressions.

4.2.4.1 Local Heat Flux Density in the Mold

Fig. 4.9 shows two sets of data of the local heat flux density along the length of the mold.[11,12] There is a maximum of the heat flux density somewhat below the meniscus. Downward the heat flux density usually decreases. However, the curve is not always smooth as in Figs. 4.9a and b; that is, there can be oscillations. Also, a plateau may be reached or there may be an increase again at the lower end of the mold (Fig. 4.9b), which occurs if the gap thickness decreases in the lower part of the mold or if contact is established again. If the gap between the mold and strand is of approximately uniform thickness, or if it increases uniformly in the downward direction (that is, if the conicity of the mold and the guidance of the strand below the mold are correct), the decrease of the heat flux density along the length of the mold is continuous and according to a smooth curve. To a good approximation, straight lines result in half-logarithmic plots. Examples are shown in Fig. 4.10. Hence, q can be described, for the normal operation, by the exponential law:[10]

$$q = q_a\, e^{-\alpha z} \qquad \text{(Eq. 4.28)}$$

The exponent α, which results from the slope of the straight lines, is usually about 0.0015 mm^{-1}. Further, the data demonstrate that the heat flux increases with increasing casting velocity v_c. This effect and the decrease down the mold are caused partially by the increase of the heat resistance of the solid steel shell. The shell thickness decreases with increasing strand velocity, at given distance z from the meniscus, due to the shorter solidification time, and it increases, of course at given casting velocity v_c, with increasing distance z from the meniscus. Also the heat resistance of the gap depends on the casting rate. It can be expected that the upper zone with the coherent layer of casting flux is extended and that, in total, the gap becomes thinner with increasing casting rate. Thus, the heat resistance of the gap decreases with increasing casting rate.

The heat flux density at the meniscus cannot be measured directly with the usual technique (determination of temperature gradient with two thermocouples) because the temperature field in the copper plate is strongly two-dimensional in this region, causing a considerable longitudinal heat flow upward to the cold top of the mold. However, apparent heat flux densities q_a at the meniscus can be obtained by extrapolation to z = 0 of the straight lines in plots according to Fig. 4.10. In Fig. 4.11a the q_a values are plotted against v_c in log-log scale. From the normalized graph in Fig. 4.11b the relationship:

$$q_a = A\, v_c^{\beta} \qquad \text{(Eq. 4.29)}$$

is deduced with $\beta = 0.56$. Hence, for the mold heat flux density the simple equation:

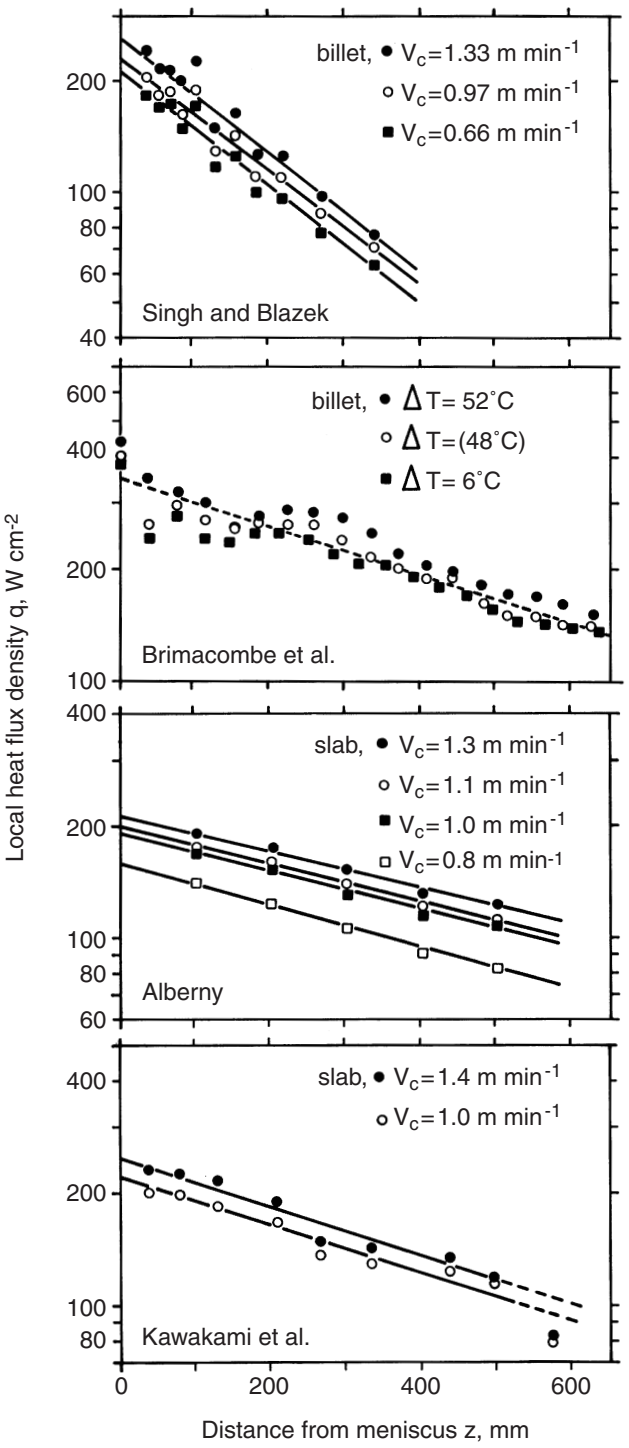

Fig. 4.10 Plot of local heat flux density in a continuous casting mold against distance from the meniscus in half-logarithmic scale, demonstrating the exponential relationship. *From Ref. 10.*

$$q_a = A\, v_c^{0.56}\, e^{-0.0015z},\ W\ m^{-2} \qquad \text{(Eq. 4.30)}$$

results, in which v_c is in m min^{-1} and z in mm. The quantity A is the apparent heat flux density at the meniscus (z = 0) if v_c = 1 m min^{-1}. It depends on additional parameters and varies considerably

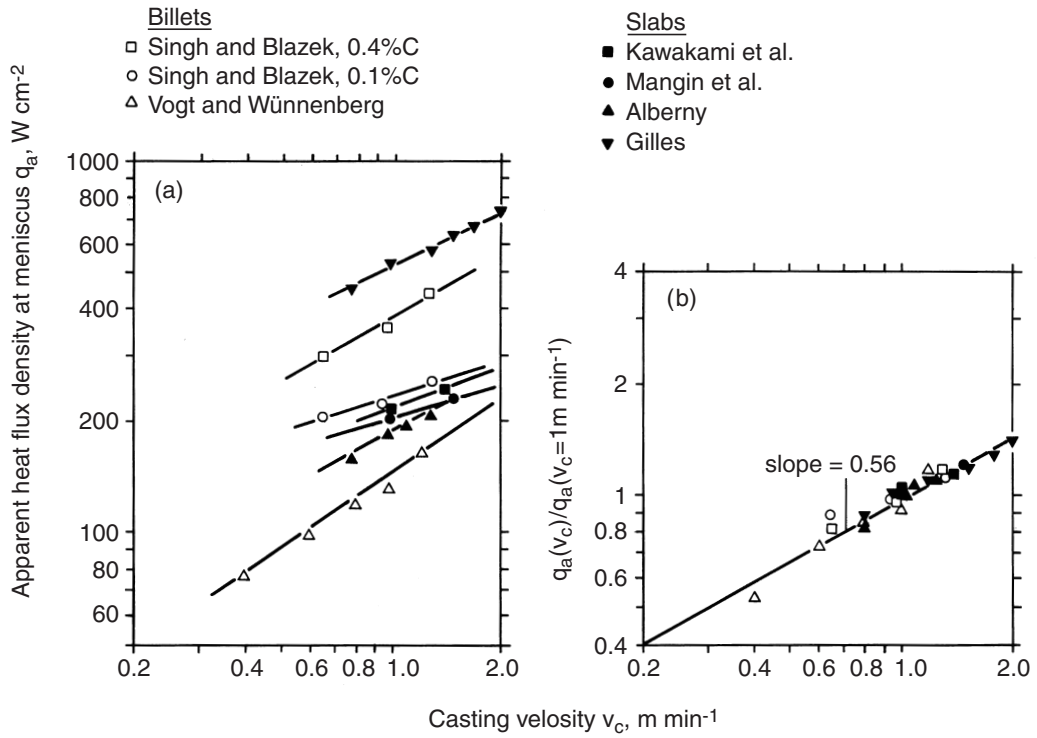

Fig. 4.11 Apparent heat flux density at the meniscus (extrapolated) as a function of casting rate. *From Ref. 10.*

for different machines and casting practices (see Fig. 4.11a). As a first number, A may be taken to be 200 W cm^{-2} (m min^{-1})$^{-0.56}$.

In the data evaluation leading to equation 4.30, it was assumed that the local heat flux density depends on the two independent variables z and v_c. Alternatively, it may be expected that, in an approximate manner, the local heat flux density is a function of the time t of travel of a strand slice from the meniscus to the location z. Hence, in this case the two variables z and v_c are combined into the single variable $t = z/v_c$ and expressions of the forms:

$$q = A\, t^{-\gamma} \qquad \text{(Eq. 4.31)}$$

$$q = A - B\, t^{0.5} \qquad \text{(Eq. 4.32)}$$

$$q = A - B\, t + C\, t^2 - D\, t^3 + E\, t^4 \qquad \text{(Eq. 4.33)}$$

$$q = A\, e^{-\gamma t} + B \qquad \text{(Eq. 4.34)}$$

have been used where A to E are constants.[12–15] For instance, Fig. 4.12 shows the data of Fig. 4.9b plotted as a function of t, and indeed the points for the different casting velocities fall fairly well on a single curve given by:

$$q = 722\, t^{-0.558} \qquad \text{(Eq. 4.35)}$$

where q is in W cm^{-2} and t in s. The correlations with t can be justified theoretically if the heat transfer coefficient caused by the gap is a sole function of t; that is, the physical state of the gap changes with z and v_c according to z/v_c, which, of course, is not strictly so in reality. There is also the practical problem that the apparent heat flux density at the meniscus (value of q at t = 0) is independent of casting velocity v_c according to equations 4.32 to 4.34, which is not in accord with the

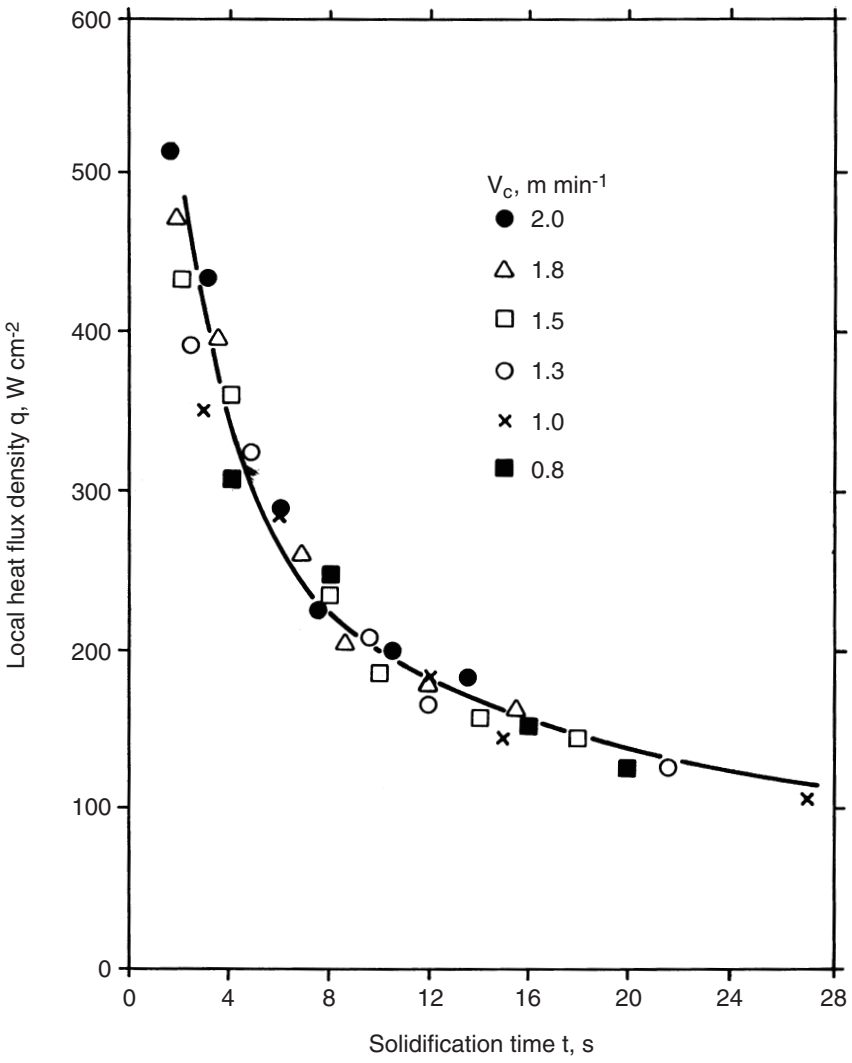

Fig. 4.12 Heat flux density data of Fig. 4.9b plotted against $t = z/v_c$. *From Ref. 12.*

extrapolated data (see Fig. 4.11a) and for which is hard to imagine why it should, or that it becomes infinite according to equation 4.31.

4.2.4.2 Average Heat Flux Density in the Mold

The average heat flux density $\bar{q}$ can be computed from the increase of cooling water temperature ΔT_w, via the formula:

$$\bar{q} = \frac{Q \rho c_p \Delta T_w}{L_m W} \qquad \text{(Eq. 4.36)}$$

where Q is the volume rate of the cooling water, ρ the density (997 kg m^{-3} at 25°C), c_p the heat capacity of water (4180 J kg^{-1} at 25°C), L_m the mold length in contact with the strand (normally 600 mm) and W the perimeter of the tube mold (billet mold) or the width of a mold face with separate cooling circuit (slab mold). The average and local heat flux densities are interrelated by:

$$\bar{q} = \frac{1}{L_m} \int_0^{L_m} q \, dz \qquad \text{(Eq. 4.37)}$$

and the expression corresponding to equation 4.28 is:

$$\bar{q} = \frac{q_a}{L_m} \int_0^{L_m} e^{-\alpha z}\, dz = \frac{q_a}{\alpha L_m}(1 - e^{-\alpha L_m}) \qquad \text{(Eq. 4.38)}$$

and with equation 4.29

$$\bar{q} = \frac{A\, v_c^{\beta}}{\alpha L_m}(1 - e^{-\alpha L_m}) \qquad \text{(Eq. 4.39)}$$

Fig. 4.13 shows experimental data for $\bar{q}$ as a function of v_c.[16–23] The two lines representing equation 4.39, one for L_m = 600 mm and the other for L_m = 900 mm (high speed casting), are included for comparison.

Alternatively, if the solidification time t is used instead of distance z, the local and the average heat flux densities are interrelated by:

$$\bar{q} = \frac{1}{t_m} \int_0^{t_m} q\, dt \qquad \text{(Eq. 4.40)}$$

where $t_m = L_m/v_c$ is the time of residence in the mold of a downward-traveling strand slice (dwell time). From equations 4.31 and 4.32 we get the following:

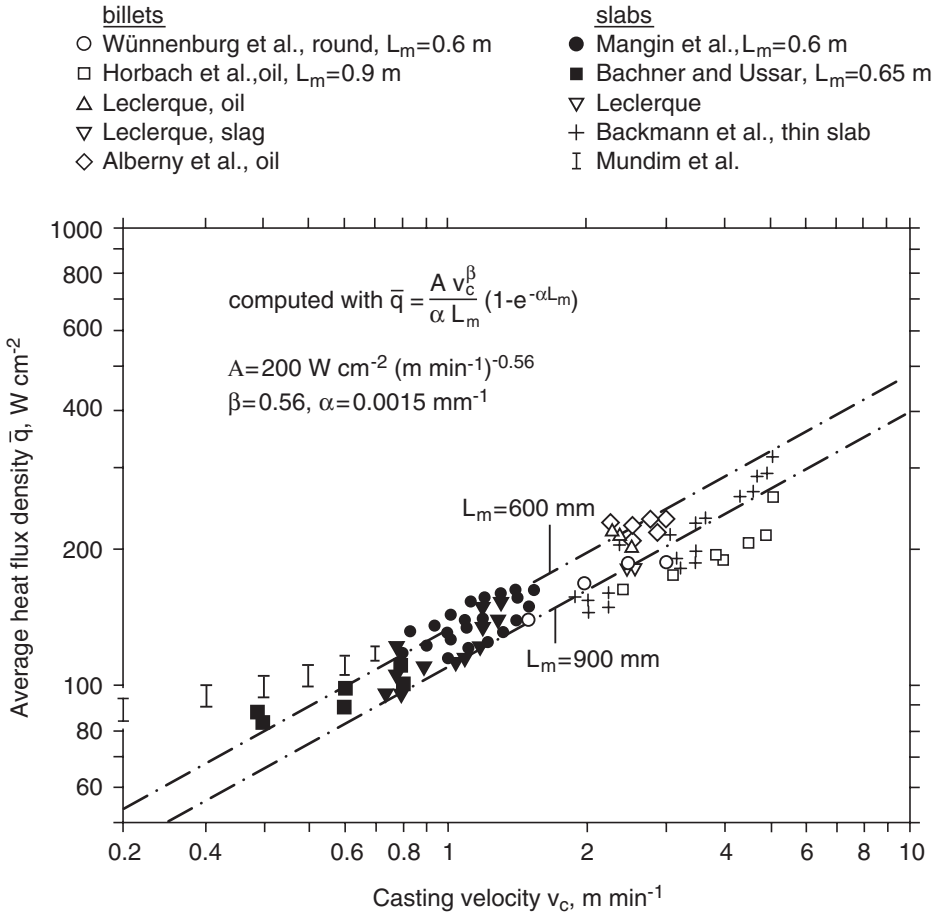

Fig. 4.13 Plot of average heat flux density versus casting speed. *From Refs. 16–23.*

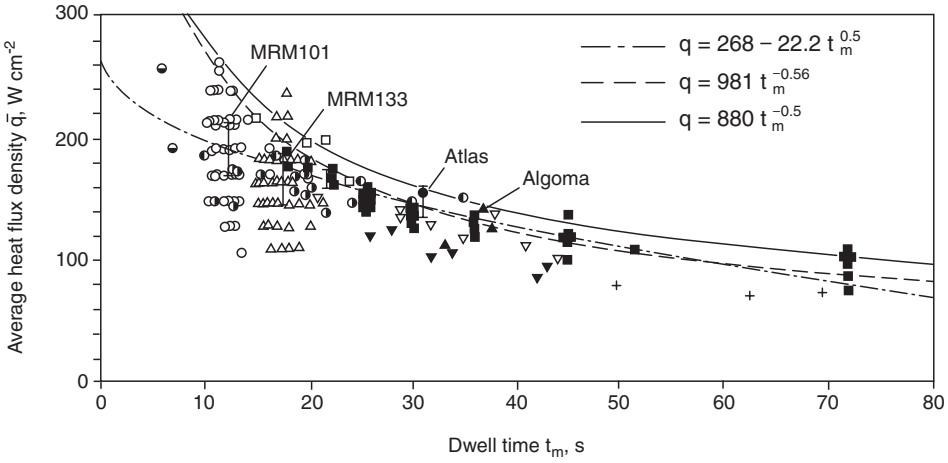

Fig. 4.14 Plant data of average heat flux density in the mold as a function of dwell time. *From Ref. 24.*

$$\bar{q} = \frac{A}{1-\gamma}\, t_m^{-\gamma} \qquad \text{(Eq. 4.41)}$$

or

$$\bar{q} = A - \frac{B}{1.5}\, t_m^{0.5} \qquad \text{(Eq. 4.42)}$$

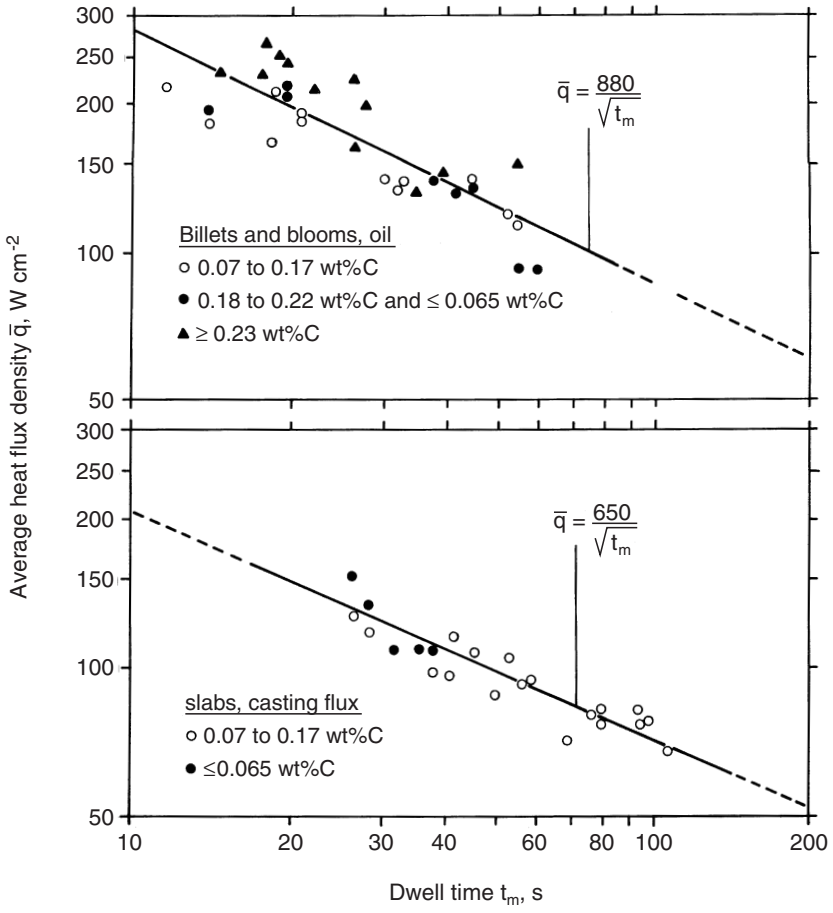

Fig. 4.15 Plant data of average heat flux density in a mold as a function of dwell time. *From Ref. 25.*

Equations of the form of 4.41 and 4.42 have been used by many authors. Figs. 4.14 and 4.15 show sets of data collected by Lait et al.[24] and by Wolf,[25] respectively, which have been represented by the authors with the equation:[24]

$$\bar{q} = 981\, t_m^{-0.56}\ ,\ W\ cm^{-2} \qquad \text{(Eq. 4.43)}$$

with t_m in s:[25]

$$\bar{q} = 880\, t_m^{-0.5}\ ,\ W\ cm^{-2}\ \text{(billets, oil lubrication, 0.05 to 0.75\% C)} \qquad \text{(Eq. 4.44)}$$

$$\bar{q} = 650\, t_m^{-0.5}\ ,\ W\ cm^{-2}\ \text{(slab, flux lubrication, 0.03 to 0.17\% C)} \qquad \text{(Eq. 4.45)}$$

Note that equation 4.43 cannot be valid at large t_m, that is, for long molds and low casting rate. ($\bar{q}$ becomes 0 for t_m = 146 s and negative for t_m > 146 s.) Equation 4.39 yields, with $v_c = L_m/t_m$ and using L_m = 600 mm and A = 200 W cm^{-2} (m min^{-1})$^{-0.56}$:

$$\bar{q} = 981\, t_m^{-0.56}\ ,\ W\ cm^{-2} \qquad \text{(Eq. 4.46)}$$

and

$$\bar{q} = 1633\, t_m^{-0.558}\ ,\ W\ cm^{-2} \qquad \text{(Eq. 4.47)}$$

In Fig. 4.14 the curves given by equations 4.44 and 4.46 are drawn in addition to that representing equation 4.43, for the comparison. In the range of practical importance 20 s < t_m < 60 s, the different correlations are close to each other. Equation 4.47 gives higher values.

4.2.4.3 Influence of Other Factors on the Heat Flux Density in the Mold

The casting flux has an influence on the mold heat flux density.[16,21,26] The thicker the flux layer between the strand and the mold, the larger will be its resistance to heat transfer. It can be assumed

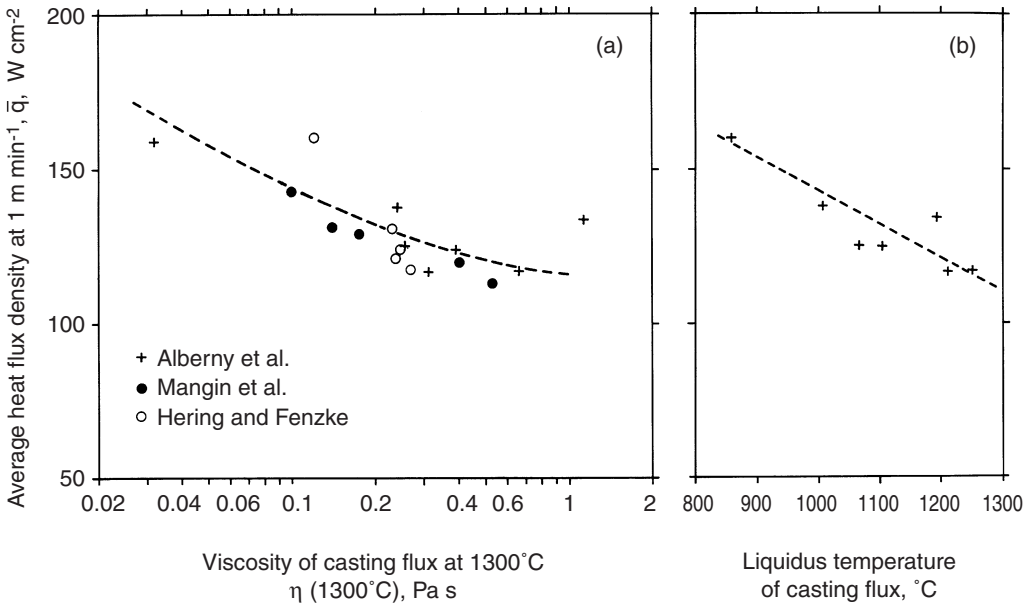

Fig. 4.16 Influence of properties of casting slag on average heat flux density. *From Refs. 16, 21, 26.*

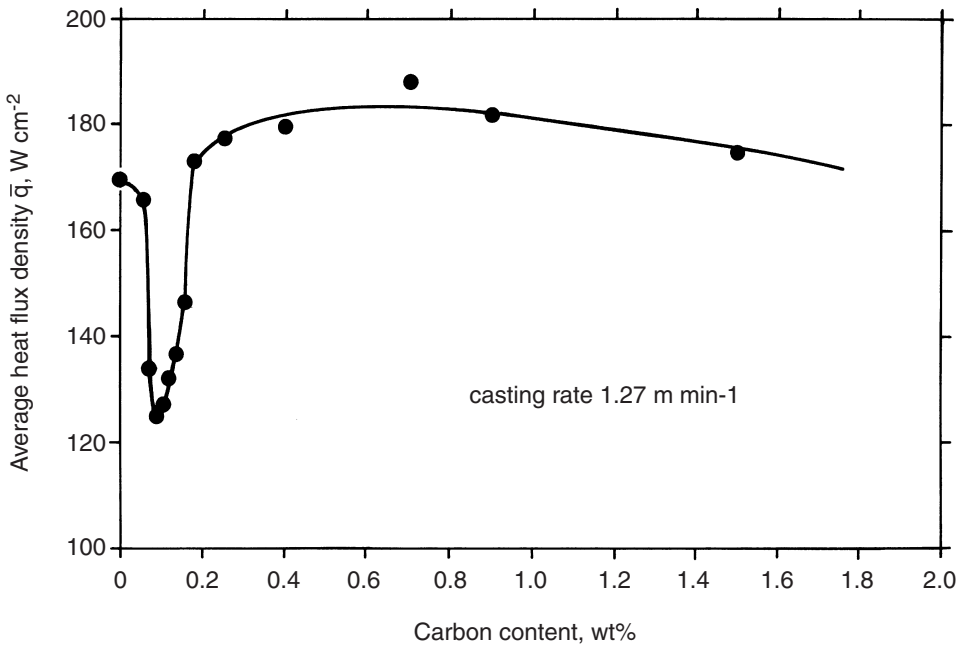

Fig. 4.17 Influence of carbon content on average heat flux density in a billet mold. *From Ref. 27.*

that the casting flux layer thickness (d_{cf} in Fig. 4.2) increases with increasing viscosity of the flux. Hence, it seems reasonable that the heat flux density decreases with increasing viscosity. Also, the melting point of the casting flux has an effect on the thickness of the flux layer and on the length of the coherent layer zone. Fig. 4.16 shows data of the average heat flux density at 1 m min^{-1} plotted against viscosity at 1300°C, or against liquidus temperature of the flux. The points of Alberny[16] refer to the same experiments. There are no data in which viscosity and melting range have been varied independently. The diagrams in Figs. 4.16a and b show the expected behavior. However, it cannot be deduced which fraction of the change of q is the viscosity or the temperature effect.

There is also a difference of heat transfer between casting with slag or with oil, the latter exhibiting higher heat flux densities. This effect is evident from the two diagrams in Fig. 4.15.[25]

In billet casting, a minimum of heat flux density has been found by several authors at carbon contents of about 0.1 wt%[18,28–30] (see Fig. 4.17). It is believed that this minimum is due to the specific shrinkage behavior of such steels (peritectic transformation). It is not so clear whether such an effect exists in slab casting.

Of course, the geometrical details of the mold, the material and the water flow rate influence heat extraction. There is a rather strong effect of taper (billet, bloom), which has already been mentioned in the context of Fig. 4.9. Molds tapering slightly inward minimize the harmful effect of the gas gap. Fig. 4.18 shows an increase of heat extraction by about 13% between 0 and 1% taper (area related).[31] In slab casting the heat flux density may be different at the wide and narrow faces. Also, bulged molds used in thin-slab casting may exhibit increased heat transfer locally and in the average. The mold material plays a role. The comparatively low heat flux densities in Fig. 4.9a were probably due to the steel mold used instead of the normal copper mold. Platings, coatings and groovings are used (or have been tried out) for different reasons and usually cause decreased heat flux densities. There are many special effects that cannot be treated in this discussion.

4.3 Heat Withdrawal in the Secondary Cooling Zone

In the upper part of the secondary cooling zone, the strand is usually sprayed by water emerging from nozzles arranged in the spaces between the rolls. Heat transfer is rather complex, involving

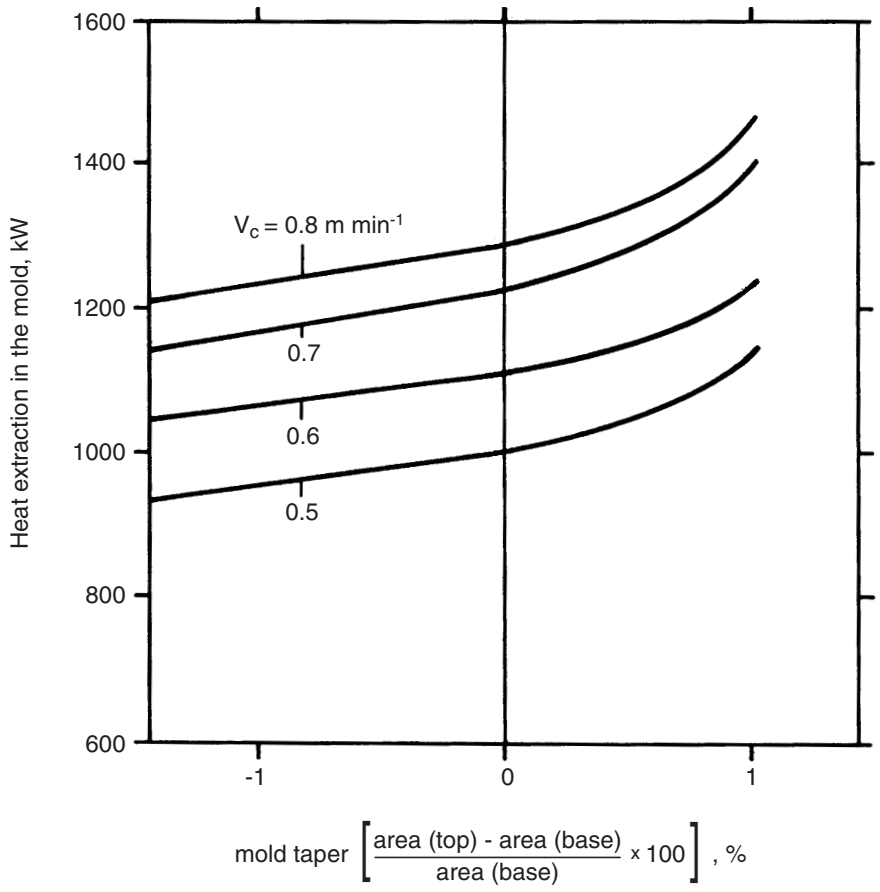

Fig. 4.18 Influence of taper on average heat flux in the mold. *From Ref. 31.*

several mechanisms. Fig. 4.19 shows a roll pair with the different cooling zones that are, in addition to the zone of direct spray impingement, the zones of the downward-flowing water, of the water pool formed above the lower roll, of contact between roll and strand, and of dry cooling at the strand surface that is not reached by the water. In the lower part of the secondary cooling zone, heat transfer is mainly by radiation and by roll contact. Some modern continuous casting plants apply no water sprays at all in the secondary cooling zone; that is, cooling is by radiation and by roll contact over the whole surface of the strand below the mold. In such a practice the rolls are internally water cooled.

Some of the mechanisms of cooling are fairly well understood, e.g., cooling by sprays; others have not been investigated in detail. The state of the knowledge is described in the subsequent sections.

4.3.1 Spray Cooling

There are two main types of nozzles, according to the shape of the wetted area: flat jet nozzles used in slab casting and cone nozzles used in billet and bloom casting. The wetted area in the first type is in the form of a rectangle with small rounded sides; that of the second type is in the form of a circle (full cone nozzle). There are also two types according to the discharge media: conventional nozzles for discharge of only water and nozzles for discharge of air-water mixtures (air-mist nozzles), where the water emerging from the nozzle disintegrates into a cloud of small droplets. The average droplet size may vary between 100 and 1000 μm, with the air-mist nozzles making smaller droplets. The water flux density impinging on the target (in the form of droplets) is more or less nonuniform over the sprayed area, depending on nozzle design. Its average value decreases with increasing distance between nozzle and target, because the sprayed area becomes larger and

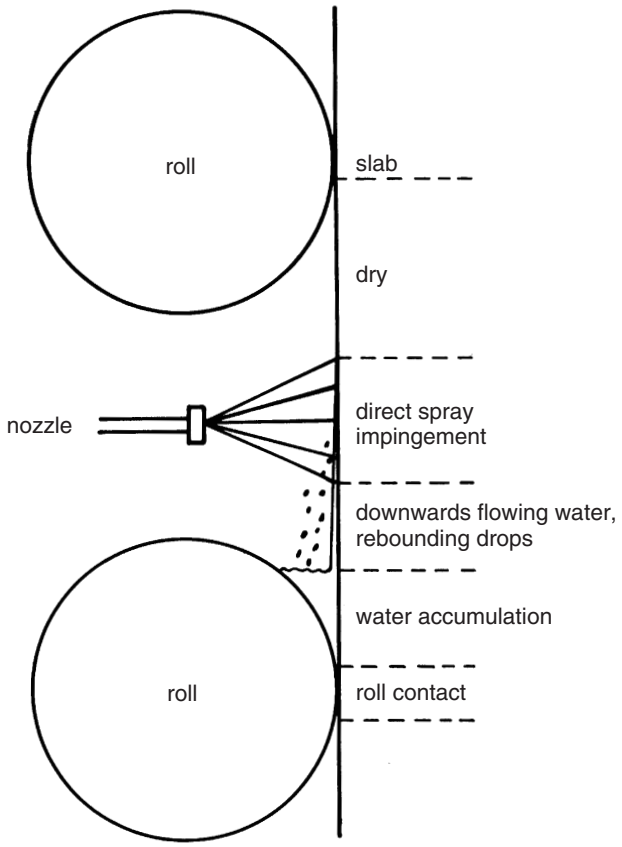

Fig. 4.19 Regions with different heat transfer mechanism between a roll pair in the spray zone of a slab caster.

increases with the water pressure in the nozzle.

In the following section, heat flux data are given. It will be evident that the heat flux density at the strand surface is influenced considerably by the features of the spray system. Hence, the spray pattern details for the nozzles used are very important and must be known for proper control of strand cooling in the secondary cooling zone.

4.3.1.1 Heat Extraction by Water Spray Nozzles

In spray cooling the evaporation of water plays an important role. The same characteristic heat transfer curve with a maximum and minimum is observed as discussed in Section 4.2.3.1, but the maximum and minimum are at much higher temperatures. A typical heat flux versus temperature relationship is shown in Fig. 4.20.[32] There is a maximum of heat flux density at low temperature, corresponding to the burn-out point in Fig. 4.6, and a critical temperature at which the range of stable film boiling commences, corresponding to the Leidenfrost temperature. The cooling characteristics of spray nozzles have been measured by numerous authors. The data are presented in various forms: as the total heat flux density q_t, as the heat flux density q_s due to the effect of the

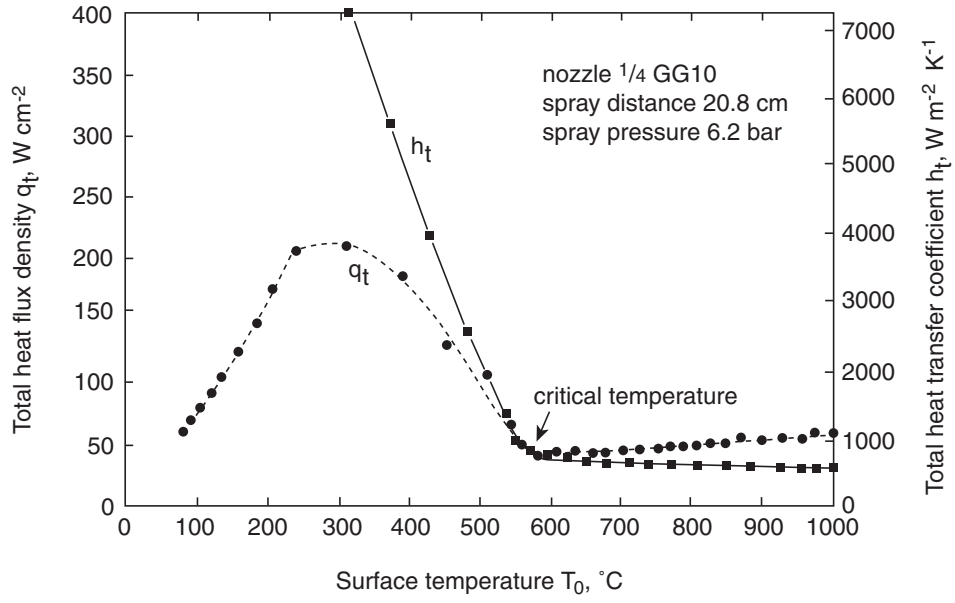

Fig. 4.20 Typical heat flux versus temperature relationship in water spray cooling. *From Ref. 32.*

spray (which is the total heat flux density q_t minus that due to radiation q_r), as a total heat transfer coefficient h_t and as a spray heat transfer coefficient h_s.

The heat transfer coefficients are usually related to the difference between the surface temperature T_0 and the water temperature T_w, that is:

$$h_t = \frac{q_t}{T_0 - T_w} \qquad \text{(Eq. 4.48a)}$$

and

$$h_s = \frac{q_s}{T_0 - T_w} \qquad \text{(Eq. 4.48b)}$$

However, sometimes it is related to the difference between the temperature T_0 and the boiling point of water T_{bp}. The radiative heat flux density is usually taken as:

$$q_r = \varepsilon\sigma (T_0^4 - T_w^4) \qquad \text{(Eq. 4.49)}$$

This may be a satisfactory approximation. Also $(T_0{}^4 - T_{bp}{}^4)$, with T_{bp} being the boiling point of water, has been used as the driving force; however, this does not make much of a difference in comparison to equation 4.49. Correspondingly, the radiative heat transfer coefficient is:

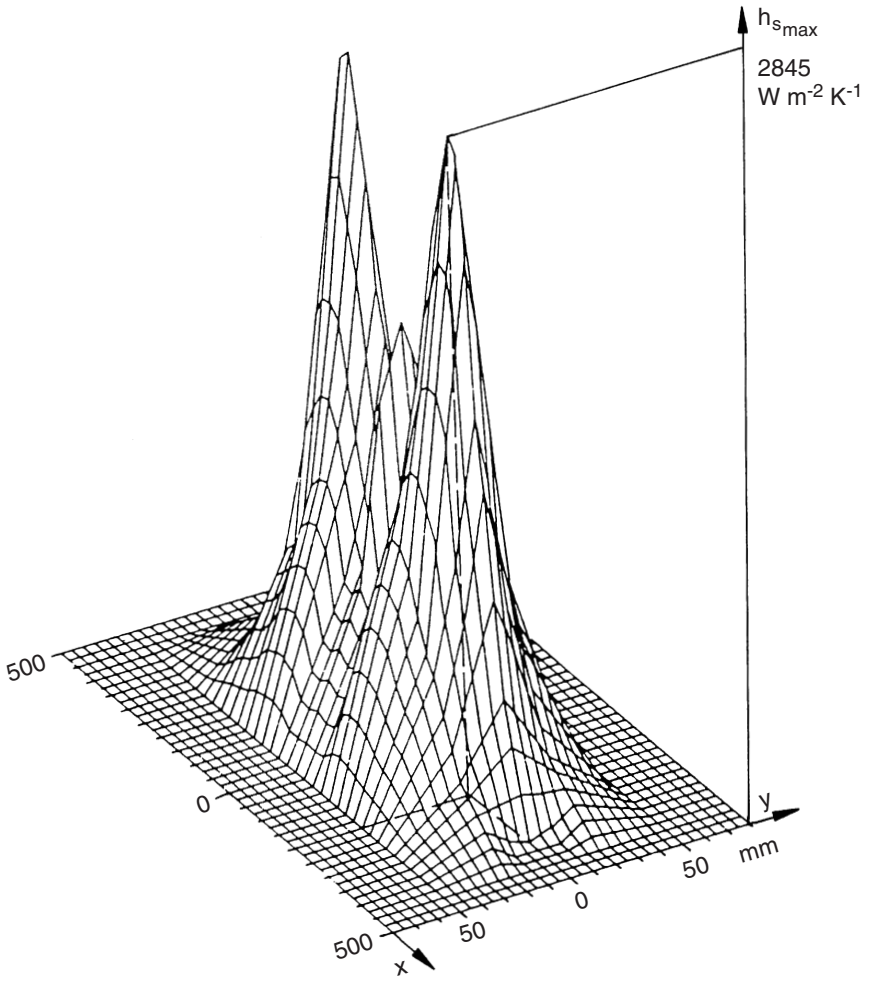

Fig. 4.21 Variation of heat transfer coefficient with position on sprayed target. *From Ref. 35.*

$$h_r = \varepsilon\sigma\,(T_0^2 - T_w^2)(T_0 + T_w) \qquad \text{(Eq. 4.50)}$$

Note that in equations 4.49 and 4.50 all temperatures must be in K. The total heat flux density q_t and the total heat transfer coefficient h_t are obtained by adding the radiation parts given in equations 4.49 and 4.50:

$$q_t = q_s + q_r \qquad \text{(Eq. 4.51)}$$

$$h_t = h_s + h_r \qquad \text{(Eq. 4.52)}$$

The data available for the heat transfer coefficients or heat flux densities have been reviewed and brought into common correlations by several authors.[10,33,34] The main factor controlling the heat transfer rate apart from the surface temperature T_0 is the water flux density V_w. Since the water flux density varies locally on the target, the heat flux density and heat transfer coefficient are also local quantities. Fig. 4.21 shows a typical example for the variation of h_s with position on the target.[35] Unfortunately, the local variation of the heat transfer rate has not been recognized by all authors; that is, measurements were performed with rather large probe areas so that conditions were nonuniform over the area of the probe, or it is unclear on the whole whether local values or averages over some area were reported.

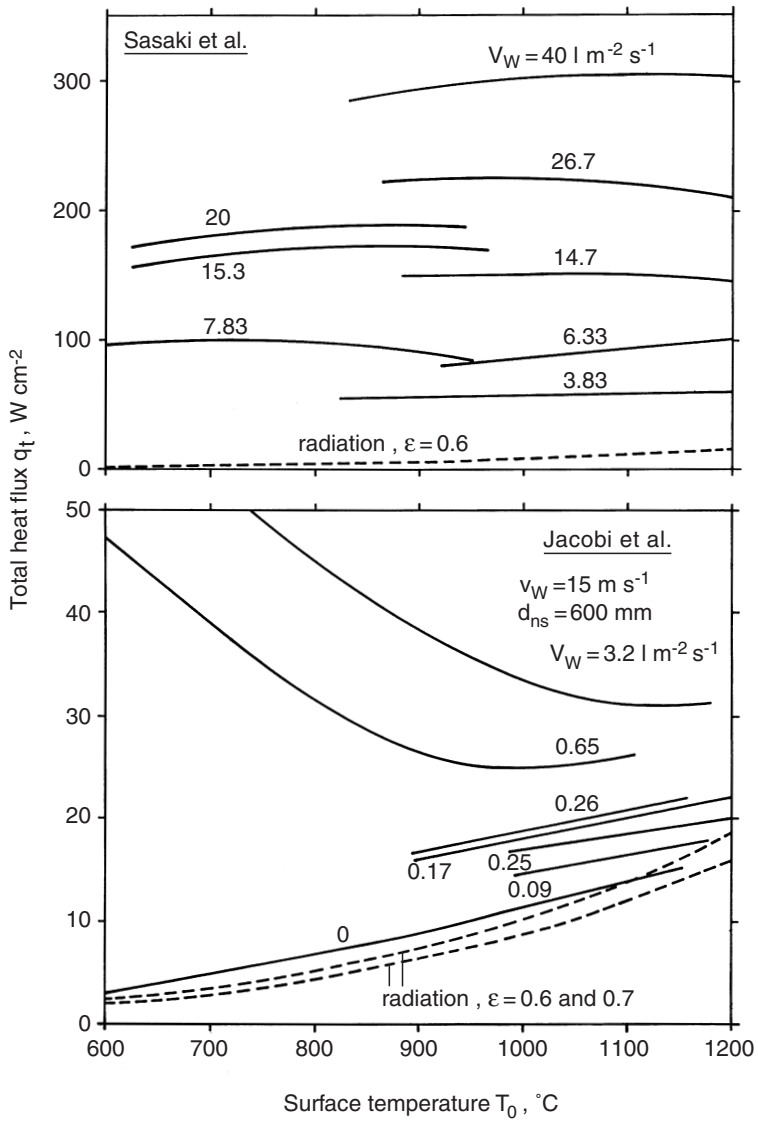

Fig. 4.22 Heat flux density under the spray nozzle as a function of surface temperature and water flux density: (a) *from Ref. 36;* (b) *from Ref. 37.*

As is evident already from Fig. 4.20, the heat flux density is a strong function of temperature, particularly at lower temperatures. It is not clear, however, in which manner the heat flux density varies with temperature in the range of continuous casting, that is, above about 700°C. Depending on the author it may be practically independent of T_0,[36] or it may increase[31,38,39] or still decrease somewhat with increasing T_0. The heat transfer coefficients are often taken to be practically temperature-independent. But most authors find a decrease with increasing T_0. Since the heat transfer coefficient seems to be temperature-dependent and, in fact, there is no reason why it should not be so, it may be more appropriate to report the directly measured q (T_0)

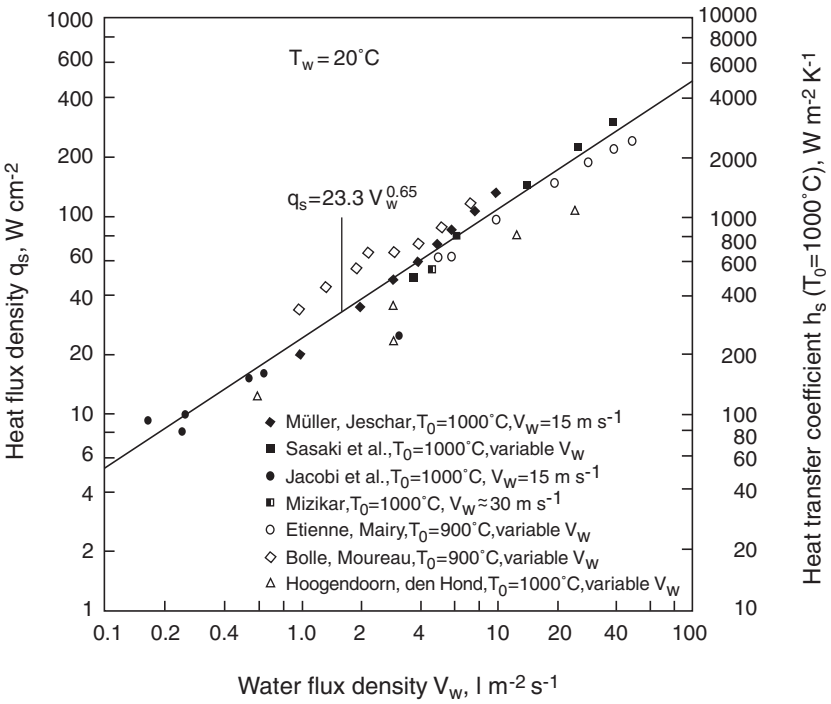

Fig. 4.23 Heat flux density (without contribution of radiation) under a spray nozzle as a function of water flux density. *From Refs. 31, 36–39, 41.*

functions rather than convert them into h (T_0) functions. Fig. 4.22 shows examples of the measured heat flux density versus temperature relationships. The strong effect of water flux density V_w is clearly evident. The data of many authors can be brought together in the temperature range above about 900°C by plotting the spray heat flux density q_s against the water flux density V_w.[10] Such a diagram in double-logarithmic scale is shown in Fig. 4.23, yielding a correlation $q_s = 23.3\ V_w^{0.65}$ with q_s in W cm^{-2} and V_w in 1 m^{-2} s^{-1}. V_w contains the effect of distance between nozzle and target; that is, changing the distance affects q_s via the changing value of V_w.

Though V_w is the most important parameter controlling q_s above about 900°C, there are also effects from the velocity of the water at the nozzle exit and from the water temperature T_w. The water velocity v_w is related to the water pressure in the nozzle Δp according to $v_w \sim \Delta p^{1/2}$. Figs. 4.24a and

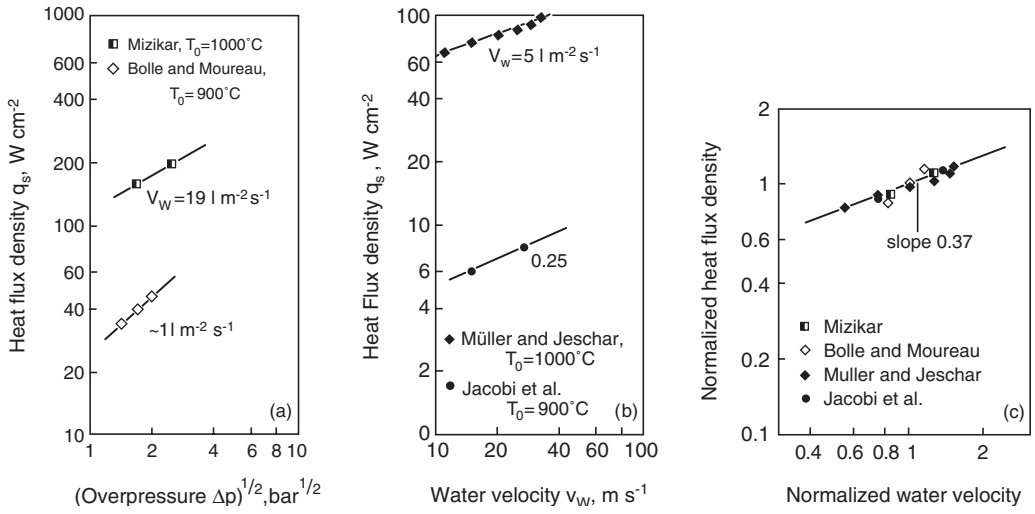

Fig. 4.24 Heat flux density under spray nozzle (without contribution of radiation) as a function of pressure at the nozzle or of water velocity: (a) and (b) are original literature data *(from Refs. 31, 37–39)*; (c) normalized heat flux density versus normalized water velocity *(from Ref. 10)*

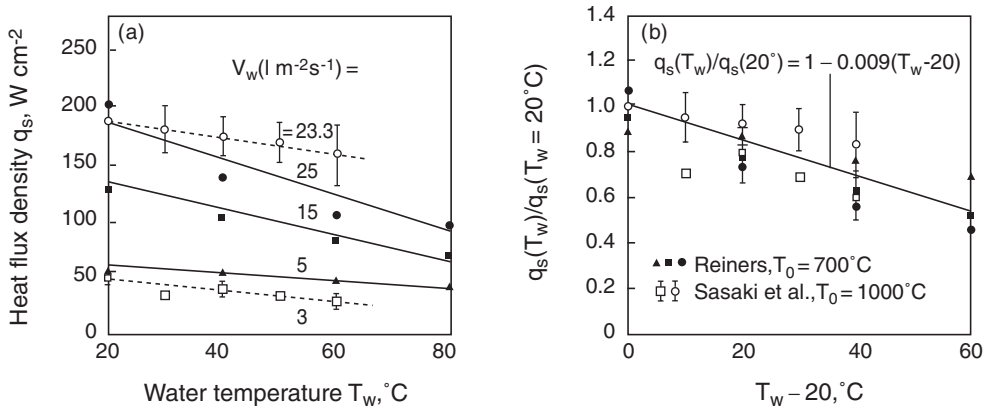

Fig. 4.25 Influence of temperature of cooling water T_w on heat flux density (without contribution of radiation under spray nozzle: (a) original literature data *(from Refs. 35, 36)*; (b) normalized heat flux versus difference of water temperature with respect to 20°C.

b show data of different authors for the variation of q_s with $\Delta p^{1/2}$ or with v_w.[31,37–39] In Fig. 4.24c the different data are brought together into one curve,[10] showing that the influence of water velocity can be expressed as $q_s \sim v_w^{0.37}$. The available data on the effect of water temperature[35,36] are presented in Fig. 4.25, indicating that the heat flux density q_s decreases with increasing T_w, as might be expected. In Fig. 4.25b, $q_s\,(T_w)/q_s\,(T_w = 20°C)$ is plotted against $(T_w - 20)$, yielding the relationship $q_s\,(T_w)/q_s\,(T_w = 20°C) = 1 - 0.009\,(T_w - 20)$. Using $v_w = 15$ m s^{-1} as a typical value in the relationship $q_s = 23.3\,V_w^{0.65}$ established in Fig. 4.23, and the functions between q_s and v_w, and between q_s and T_w as deduced in Figs. 4.24 and 4.25, the correlation for the heat flux density q_s becomes:

$$q_s = 8.55\,V_w^{0.65}\,v_w^{0.37}\left[1 - 0.009(T_w - 20)\right],\ \text{W cm}^{-2} \qquad \text{(Eq. 4.53)}$$

with V_w in l m^{-2} s^{-1}, v_w in m s^{-1} and T_w in °C. The range of validity is T_0 = 900 to 1000°C, V_w = 0.1 to 50 l m^{-2} s^{-1}, v_w = 10 to 40 m s^{-1} and T_w = 20 to 80°C.

The corresponding equation for the heat transfer coefficient (T_0 = 1000°C, T_w = 20°C) is:

$$h_s = 87.2\,V_w^{0.65}\,v_w^{0.37}\left[1 - 0.009(T_w - 20)\right],\ \text{W m}^{-2}\,\text{K}^{-1} \qquad \text{(Eq. 4.54)}$$

It should be noted that, in actuality, the effective water velocity is that of the impinging water droplets, but in equations 4.53 and 4.54 v_w is the velocity of the water stream at the nozzle exit. Hence, it is inferred in equations 4.53 and 4.54 that v_w(effective) ~ v_w, which is only so if the distance between the nozzle and the target is small. Both the water flux density V_w and the impingement velocity v_w(effective) have the dimension of velocity. They are interrelated by $V_w = g_w\,v_w$(effective), with g_w being the volume fraction of water in the water-air mixture hitting the target.

4.3.1.2 Heat Extraction by Air-Water Nozzles

Air-mist cooling is increasingly used, although the nozzle and the feeding system (two lines for water and air, respectively) are considerably more complicated. Air-water nozzles produce much smaller droplets (mist). This brings about the advantage of more uniform and softer cooling of the strand. Hence, air-mist cooling is particularly beneficial in the continuous casting of crack-sensitive steels, such as heavy plate grades. The mixing of water and air is performed usually within the nozzle. The volumetric air/water ratio can be varied over a wide range, but typical values used are between 20 and 500 (0.02 to 0.5 Nm^3 air per liter of water).

Heat extraction by air-water nozzles occurs both via water and air. It is obvious that at high gas flow rates and low water flow rates heat transfer into air will play a significant role. A considerable

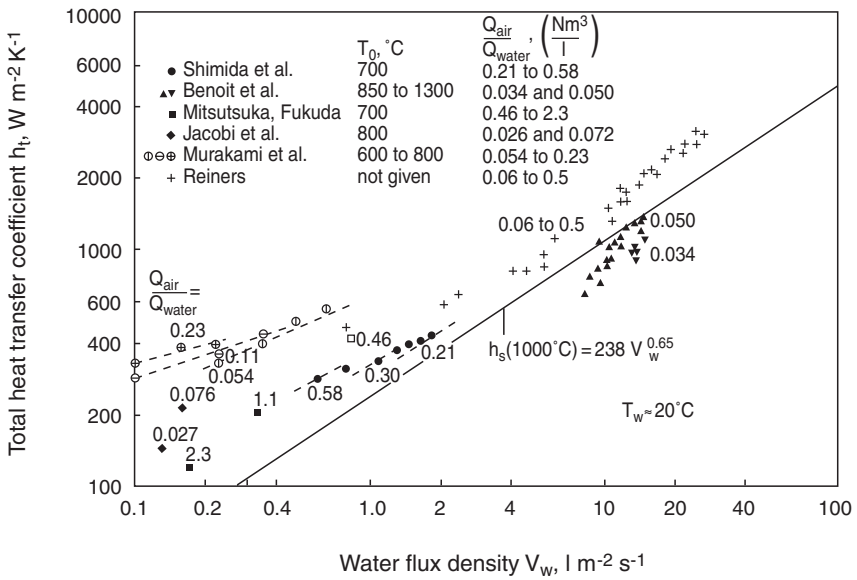

Fig. 4.26 Data on heat transfer coefficient under air-water nozzles as a function of water flux density. *From Refs. 35, 37, 42–45.*

amount of water can be replaced by compressed air without decrease in the extent of strand cooling. At high water flow rates, however, the effect of air will be small or negligible. Hence, for air-mist strand cooling the heat flux is composed of three parts, namely those related to water, air and radiation. However, in the literature the subdivision has not been performed, and total heat transfer coefficients are reported instead. The gas flows used have been given in various terms, such as air flow rate at the nozzle exit, air/water ratio at the nozzle exit, air momentum, air flux density (being unclear as to how this is computed) or impingement velocity. Unfortunately, it is not possible to deduce from the data the functional relationship between the heat flux density (heat transfer coefficient) and the variables relevant for the two phases. In Fig. 4.26 the available data on the total heat transfer coefficient[35,37,42–45] have been plotted against the water flux density V_w, with the Q_{air}/Q_{water} ratios at the nozzle given in Nm^3 l^{-1}. Included in the diagram is the relation $h_s = 238\ V_w^{0.65}$ for the only-water spray, which is equivalent to the relation $q_s = 23.3\ V_w^{0.65}$ (at $T_0 = 1000°C$, $T_w = 20°C$, h_s in W m^{-2} K^{-1} and q_s in W cm^{-2}) given in Fig. 4.23. At low V_w the heat transfer coefficients for air-mist jets are above this line, indicating the effect of the air. The data of individual authors[45] show the increase of h_t with Q_{air}/Q_{water} at a given V_w, but for all the data together this obvious effect disappears in the large scatter.

4.3.2 Dry Cooling

As already mentioned, the cooling of the strand in the lower dry part of the secondary cooling zone is mainly by radiation. The expressions for the heat flux density and the heat transfer coefficient are given as equations 4.49 and 4.50. The emissivity values used range from 0.6 to 0.8. Heat transfer is also due to natural convection, but this part is rather small compared to the radiation part.

Air jets have also been used for strand cooling. In this case there is an additional part of heat transfer by forced convection, which may approach that of radiation depending on the parameters of the jet.

The dimensionless relationships for natural convection heat transfer are given in the form Nu = f (PrGr), with Nu = Nusselt number, Pr = Prandtl number, and Gr = Grashof number.[6,7] In the range PrGr $\approx 10^9$ existing in continuous casting of steel, the correlations are in the form Nu = C $(PrGr)^{1/3}$, which has the consequence that the geometrical length cancels in the expression for the heat transfer coefficient. The following equations can be derived for cooling in air, with the surface temperature T_0 ranging from 600 to 1200°C and taking the ambient air temperature T_{air} to be about 200°C:

$$\text{vertical surface: } h_{nc} = 104\lambda;\ q_{nc} = 104\lambda(T_0 - T_{air}) \qquad \text{(Eq. 4.55)}$$

$$\text{upper side of horizontal surface: } h_{nc} = 133\lambda;\ q_{nc} = 133\lambda(T_0 - T_{air}) \qquad \text{(Eq. 4.56)}$$

$$\text{lower side of horizontal surface: } h_{nc} = 180\lambda;\ q_{nc} = 180\lambda(T_0 - T_{air}) \qquad \text{(Eq. 4.57)}$$

with λ in W m^{-1} K^{-1}, h in W m^{-2} K^{-1}, q in W m^{-2}. The value of the thermal conductivity λ to be inserted is that at the mean temperature $T = (T_0 + T_{air})/2$. The typical value of q_{nc} is 0.4 W cm^{-2} (800°C), which is about 1/10 of q_r and normally can be neglected.

The dimensionless correlation for forced convection heat transfer from a hot plate cooled by an impinging gas jet with the same temperature at the nozzle exit as the ambient gas temperature can be taken to be, in principle, of the form $Nu = f(Re,Pr,D/d_{ns},r/d_{ns})$ with Re = Reynolds number at nozzle exit, D = diameter of nozzle exit, d_{ns} = distance between nozzle and plate (strand), and r = radial distance on plate (or radius of area for average Nu). Many different correlations have been presented in the chemical engineering literature. Unfortunately, they differ and are often outside the range of interest for continuous casting. It is proposed to use the following expressions for a round air jet impinging on a round hot disc:[46,47]

$$h_{fc} = 4.66\lambda\left(\frac{v_{nozzle}\,D}{r\,d_{ns}\,\upsilon}\right)^{\frac{1}{2}} \qquad \text{(Eq. 4.58a)}$$

$$q_{fc} = 4.66\lambda\left(\frac{v_{nozzle}\,D}{r\,d_{ns}\,\upsilon}\right)^{\frac{1}{2}}(T_0 - T_{air,nozzle}) \qquad \text{(Eq. 4.58b)}$$

Here, h_{fc} and q_{fc} are the average quantities over an area with radius r. The values for the kinematic viscosity υ and for the thermal conductivity λ refer again to the mean temperature $\overline{T} = (T_0 + T_{air,nozzle})/2$.

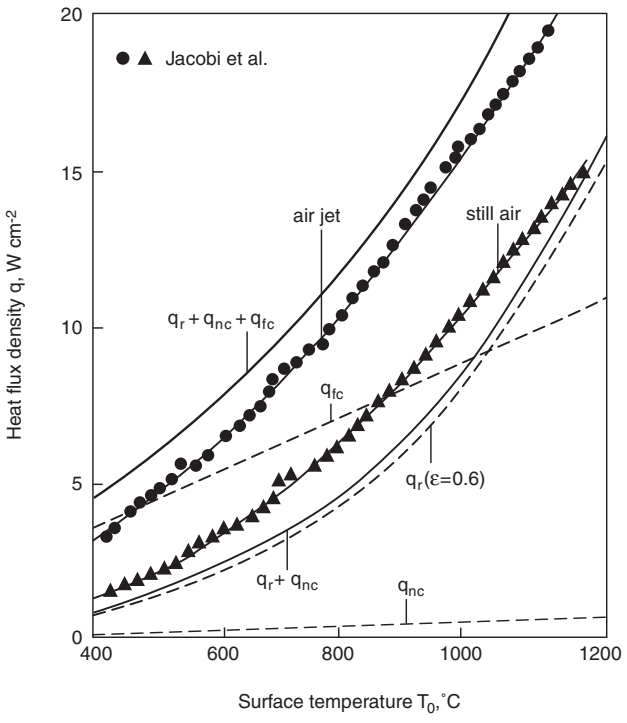

Fig. 4.27 Heat flux density in dry cooling and comparison with theoretical predictions. The data used for computation of q_{fc} were: v_{nozzle} = 773 m s^{-1}, D = 0.002 m, r = 0.22 m and d_{ns} = 0.6 m. *From Ref. 37.*

The following equations for the thermal conductivity and for the kinematic viscosity of air have been computed by application of the kinetic theory of gases:[6]

$$\text{for } 300 < T(K) < 200,\ \lambda_{air} = 3.330 \times 10^{-4}\,T^{0.7602},\ \text{W m}^{-1}\,\text{K}^{-1} \qquad \text{(Eq. 4.59)}$$

$$\text{for } 400 < T(K) < 2000 \text{ at 1 atm},\ \upsilon_{air} = 1.210 \times 10^{-9}\,T^{1.6654},\ \text{m}^2\,\text{s}^{-1} \qquad \text{(Eq. 4.60)}$$

The density of air at 1 atm is given as:

$$\rho = \frac{353.05}{T},\ \text{kg m}^{-3} \qquad \text{(Eq. 4.61)}$$

Jacobi, Kaestle and Wuennenberg[37] have investigated experimentally the cooling of a laboratory steel ingot by an impinging air jet. The nozzle was a Lechler flat jet nozzle usually applied for water spraying, and the jet of 2.43

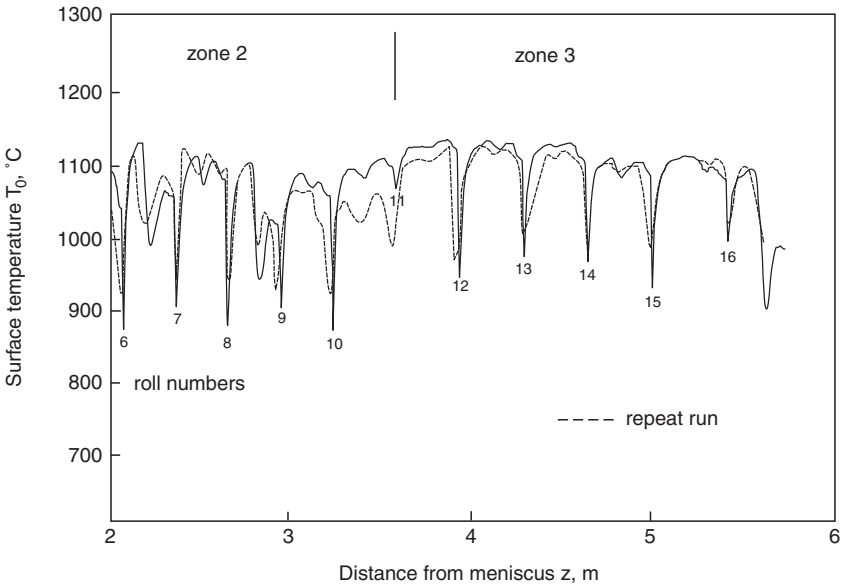

Fig. 4.28 Surface temperature along a slab strand. *From Ref. 48.*

l s^{-1} was moved to and fro over the hot area of 0.15 m^2. Hence, the conditions were not quite like those under a round fixed jet. Nevertheless, Fig. 4.27 shows that their measured heat flux densities compare favorably with computed curves for $q_r + q_{nc}$ and $q_r + q_{nc} + q_{fc}$, respectively.

4.3.3 Strand Cooling by Roll Contact

A considerable amount of heat is withdrawn in slab casting by contact of the strand with the rolls. Fig. 4.28 shows surface temperatures along the strand as measured with a traveling thermocouple.[48] The positions of the rolls are indicated by the numbers. Water sprays are between the rolls. It is seen that the temperature dips at the positions of the rolls are considerably deeper than those in the spray zones, indicating comparatively strong cooling by the rolls. The heat transfer coefficients for the roll contact zones as deduced from such temperature traces are very large in the contact zones. Data are given in Fig. 4.29. They must be computed with a two-dimensional model including the term

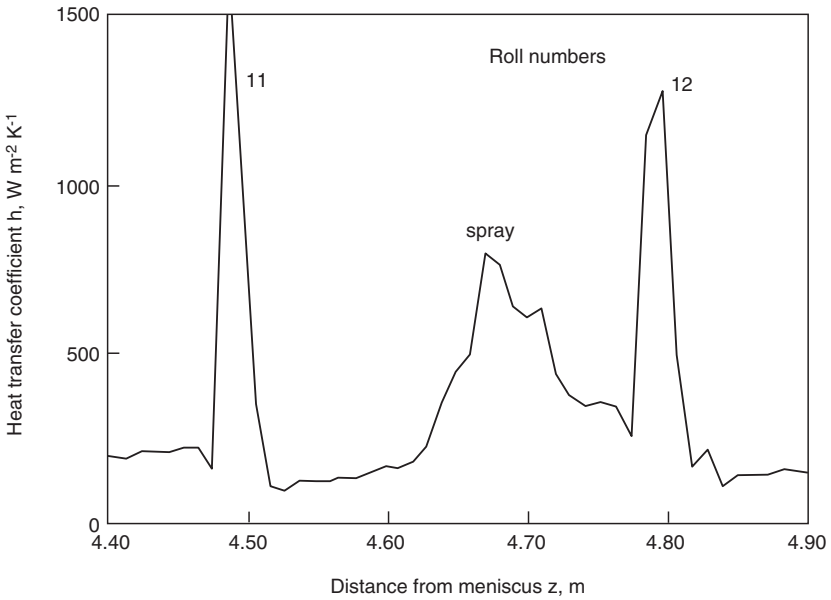

Fig. 4.29 Heat transfer coefficients deduced by application of the two-dimensional model. *From Ref. 48.*

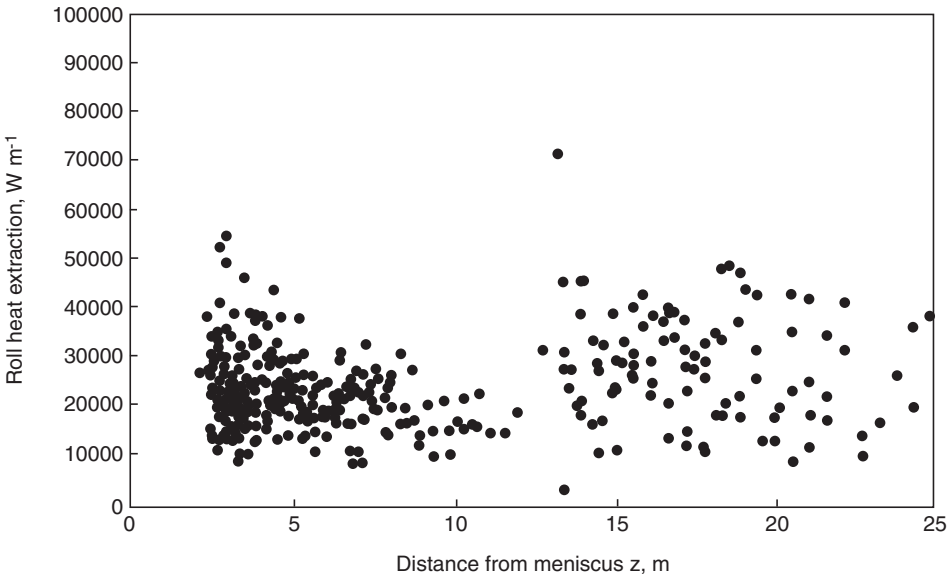

Fig. 4.30 Examples for heat extraction by the rolls. *From Ref. 48.*

$\partial(\lambda\ \partial T/\partial z)/\partial z$ (see equation 4.5 in Section 4.5) to take the conduction in the casting direction into account, which cannot be neglected if strong temperature gradients exist in the z-direction. If this is not done the heat transfer coefficients may come out zero or negative for the heat-up zone after the contact, which is clearly impossible.

The length of the contact zone depends, in principle, on many parameters (position along the strand, roll pitch, roll diameter, casting rate, spray cooling, design of rolls, and bending or misalignment state of the roll) and can hardly be predicted. Experimentally, it was found that the contact length was in the order of a few centimeters (i.e., 2 to 3 cm, Figs. 4.28 and 4.29). Fig. 4.30 shows data for heat extraction by the rolls plotted against distance from the meniscus. The scatter is large, and a variation along the strand cannot be discerned within the scatter. The data are given in terms of watt per unit width length of the slab and must be divided by an assumed contact length. The average in Fig. 4.27 is 24,800 W m^{-1}. Taking a contact length of 4 cm the heat flux density is 620 kW m^{-2}, and the heat transfer coefficient is about 600 W m^{-2} K^{-1} (average over the contact length).

Table 4.3 Typical Values for Heat Transfer Coefficients in the Secondary Cooling Zone

Zone	Source of data	Typical value for heat transfer coefficient at 1000°C (W m^{-2} K^{-1})
Dry	Eqs. 4.49 and 4.50	100
Direct spray	Eqs. 4.53 and 4.54 or data in Fig. 4.26	200–2000
Downward-flowing water		200–500
Water accumulation	From pool boiling data	1000
Roll contact		1500 (peak) 600–800 (avg.)

4.3.4 Summary

Since the heat transfer in the secondary cooling zone is complex, involving several mechanisms, the heat transfer coefficient used in models should take into account the different heat transfer zones if detailed predictions are to be made. Table 4.3 refers to Fig. 4.26 and gives equations (or diagrams) and typical values for the heat transfer coefficients.

Surface temperature variations due to the heat transfer coefficient variations are dampened in the interior of the strand and may practically disappear within a centimeter or so. If the detailed surface temperature development must not be known and/or if mainly the shell thickness and sump length are to be computed, it suffices to use average heat transfer coefficients (heat flux densities) for the regions between a pair of rolls. The average values are deduced by weighting the data for the different mechanisms according to area fractions.

4.4 Plant Data on Growth of Solid Shell

The other measurement that has been carried out in addition to that of heat flux is the determination of shell thickness. Most frequently the data are deduced from the hollows originating in breakouts.[49] Since the breakout usually occurs at the mold exit, data can be obtained only for the region of the mold and possibly somewhat below. Another method is the sensing method, in which the solid/liquid boundary in the interior of the strand is located with a mechanical sensor immersed at the meniscus in the mold.[20] Several techniques can be used to determine shell thickness along the mold and the secondary cooling zone as well. Controlled breakouts are produced by cutting (or shooting) a hole into the strand shell.[28] This technique is very expensive. Radioactive tracers (e.g., Au^{198}) or chemical tracers (FeS), which distribute in the liquid core of the strand, are added at the meniscus, thus marking the solidification front.[16,21,24,50–52] Its location along the strand is determined, after cooling to ambient temperature, by sectioning the strand and identifying the tracer. Another method is to drop a heavy pill of tungsten with an interior radiation source (Au^{198} or Co^{60}) or a lump of lead that sinks downward at a relatively high speed and settles at the bottom of the sump.[51,52] Also, a nail (or pin) of hard steel with liquidus temperature lower than that of the cast steel has been shot into the strand and melts away in the liquid.[50]

All of these methods have drawbacks. The breakout shells refer to non-normal conditions. The tracer methods can give meaningful results only if the distribution occurs very quickly over the whole of the liquid interior. Also, the lead must sink down quickly without impediment by strand curvature. Neither of the techniques gives the exact thickness of the solid shell because of the formation of the mushy zone. That is, the measured data are too large in principle and can be close to the solid shell thickness only for steels with a small solidification range, e.g., for low-carbon steels. For instance, the nail tip in the nail method melts away, depending on its liquidus and solidus temperatures and its mass, at some location within the mushy zone of the strand. The tracer methods will mark a location close to the liquidus contour because the convection is small in the interdendritic melt. Also, the breakout shells reflect some location within the mushy zone. Consequently, the shell thickness values reported for steels with large solidification ranges may be much too large. Singh and Blazek[27,28] found that the shells measured with the breakout method were considerably thicker in 0.9% C steel than in 0.05% C steel. This is very unlikely. The solid shell of the 0.9% C steel should be thinner than that of the 0.05% C steel (at the same average heat flux density) because of the increase of the mushy zone with carbon content.

Fig. 4.31 shows data of apparent shell thickness $´x_s´$ for a low-carbon steel (0.06% C) measured with the radioactive tracer method. The thickness values are plotted against distance z from the meniscus in Fig. 4.31a or against solidification time $t = z/v_c$ in Fig. 4.31b. At a given z the shell thickness increases with decreasing casting velocity v_c (see Fig. 4.31a) because of the longer traveling time (solidification time) of the shell to the position z. However, similarly as for the local heat flux density, the shell thickness values for different velocities can be combined fairly well into a

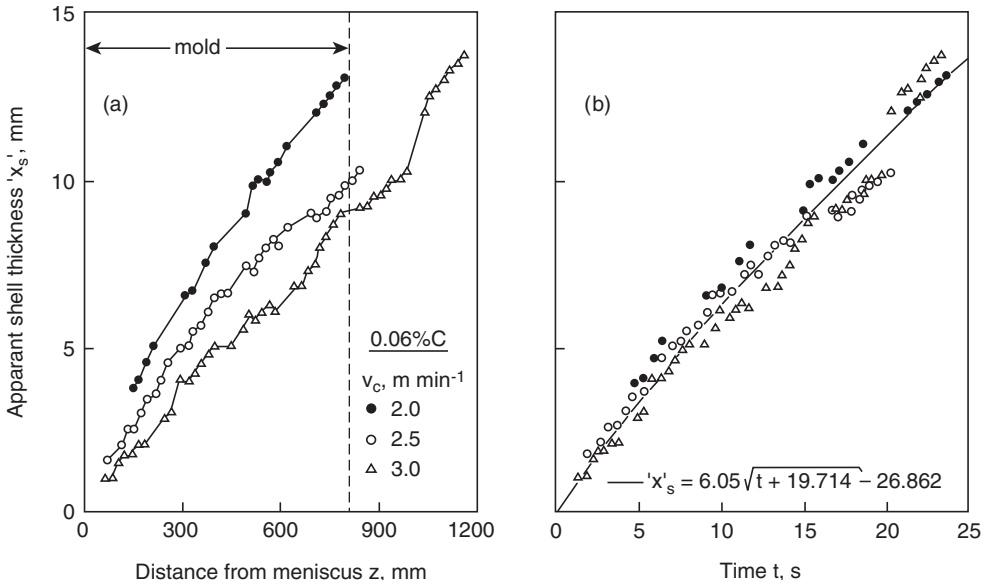

Fig. 4.31 Shell thickness of a low-carbon slab in the mold at different casting rates: (a) original data plotted against the meniscus; (b) same data plotted against solidification time $t = z/v_0$. The curve in (b) corresponds to equation 4.65.

single dependency by the plot versus time (Fig. 4.31b). It is to be remembered, however, that strictly the shell thickness and related quantities cannot be a sole function of time in normal continuous casting (see remarks with respect to the heat flux density in Section 4.2.4).

Figs. 4.32 and 4.33 show $'x_s' - t$ data for low-carbon steels[16,21,23,28,50,53,54] and for stainless steel[24,49] as reported by various authors in the log-log diagram. There is considerable deviation, particularly at small times between the various sets of data, but each set can be represented satisfactorily by a straight line indicating that the equation:

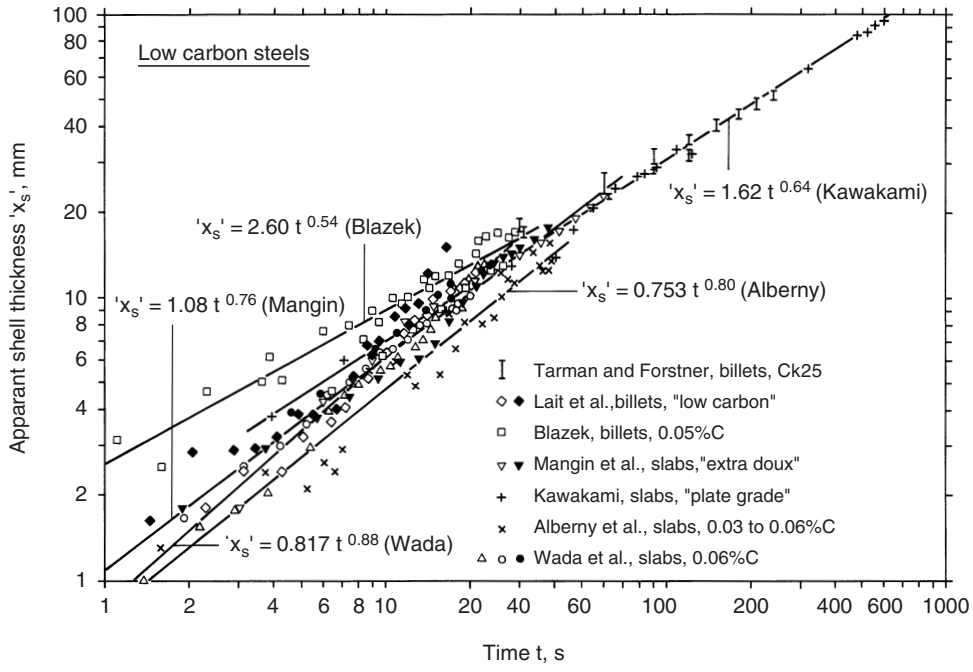

Fig. 4.32 Shell thickness data of various authors for low-carbon steels plotted against solidification time in a log-log diagram. *From Refs. 16, 21, 23, 28, 50, 53, 54.*

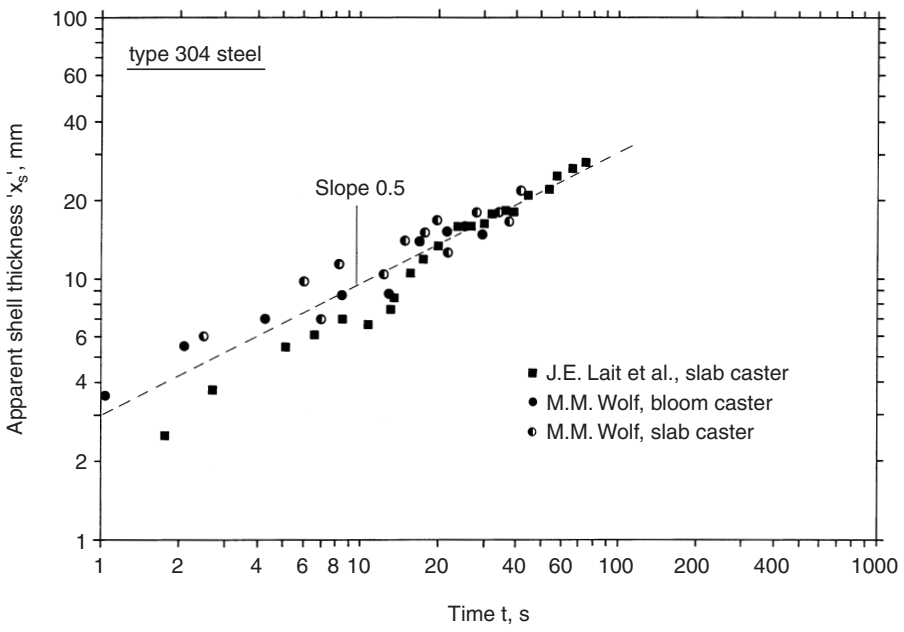

Fig. 4.33 Shell thickness data for stainless steel plotted against solidification time in a log-log diagram. *From Refs. 24, 49.*

$$´x_s´ = K´\ t^n \qquad \text{(Eq. 4.62)}$$

can be used to describe the $´x_s´$ – t relationships. The exponent n varies from about 0.5 to 0.9 depending on the author. Since at large times all the measured $´x_s´$ values converge, the larger results in a smaller K´.

Following heat flow theory, it has been customary since the early days of continuous casting to use the square root law:

$$´x_s´ = K\ t^{0.5} \qquad \text{(Eq. 4.63)}$$

for the description of shell growth. However, this equation is theoretically based on certain conditions, e.g., constant surface temperature T_0 and no superheat, which do not prevail in the real continuous casting process and in other technical solidification processes. Hence, it is not surprising that this relationship cannot be strictly fulfilled (see data in Figs. 4.31 to 4.33). Particularly in the mold region the shell growth may deviate considerably from the square root law, being often closer to a linear law. Nevertheless, in the average for the mold and for the secondary cooling zone, equation 4.63 is a convenient approximation. Apparent K-factors for the mold can be computed, of course, from the shell thickness at the exit of the mold, or at some distance z from the meniscus, and the corresponding time. K-factors range from about 12 to about 30 mm $min^{-0.5}$ for low-carbon steel. Some influences are presented below.

Modified square root laws involving two parameters K_1 and K_2 have also been used; for instance, the formula:[50,55]

$$´x_s´ = K_1\ t^{0.5} - K_2 \qquad \text{(Eq. 4.64)}$$

which, of course, is applicable only in the range $t \geq (K_2/K_1)^2$. Another form may be

$$´x_s´ = K_1\ (t + K_2^2)^{0.5} - K_1K_2 \qquad \text{(Eq. 4.65)}$$

This formula yields a linear $´x_s´$ – t function for $t \rightarrow 0$ and the square root function for $t \rightarrow \infty$. In fact, the data in Fig. 4.31b can be represented quite well by equation 4.65 with $K_1 = 6.05$ mm $s^{-0.5}$ and $K_2 = 4.44\ s^{0.5}$.

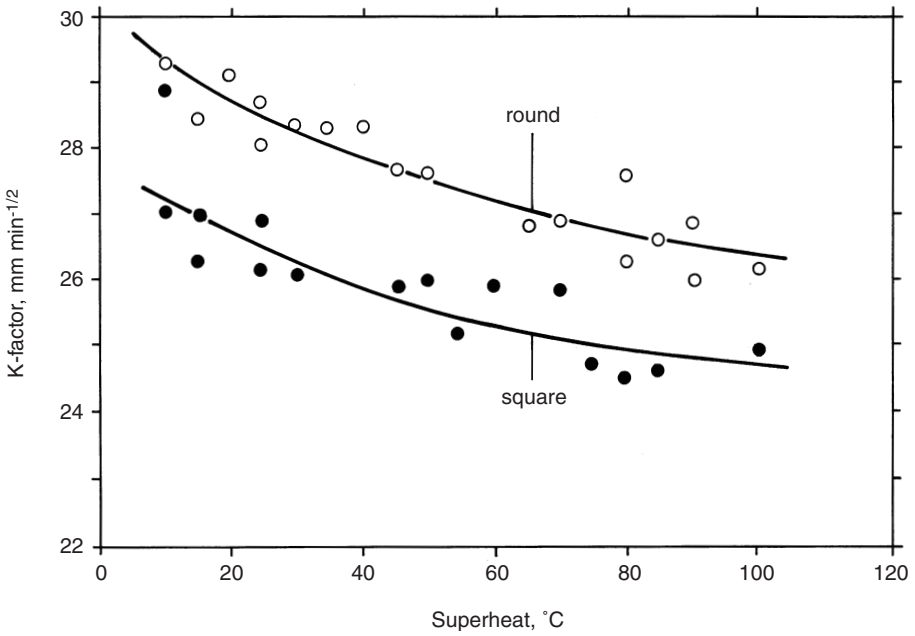

Fig. 4.34 Parabolic rate 'constant' K as a function of superheat for Ck 25. *From Ref. 54.*

4.4.1 Parameters Influencing K-factors

K-factors depend on the region of the strand for which they are evaluated. They may vary considerably along the length of the mold and the first part of the secondary cooling zone, but become fairly constant in the medium part of the secondary cooling zone. In the sump region, the rate of solid shell growth increases in billets (square and round) because the internal boundary between solid and liquid at which the heat of solidification is released continuously decreases. Hence, K-factors for the sump length are larger for billets than for slabs. The shell thickness may be rather nonuniform along the periphery of the strand at given distance from the meniscus (or given time) due to nonuniform cooling conditions. K-factors reported in the following refer to the average shell thickness.

K-factors for the mold region decrease with increasing superheat. The superheat may cause a delay of the initial solidification directly at the meniscus so that the first solid forms somewhat below the meniscus, and it definitely decreases the rate of shell growth in the upper part of the strand. Figs. 4.34 and 4.35 show K-values as reported by Tarmann and Forstner[54] and ´x_s´ values for certain times as evaluated from these data by Wolf,[25] as a function of superheat.

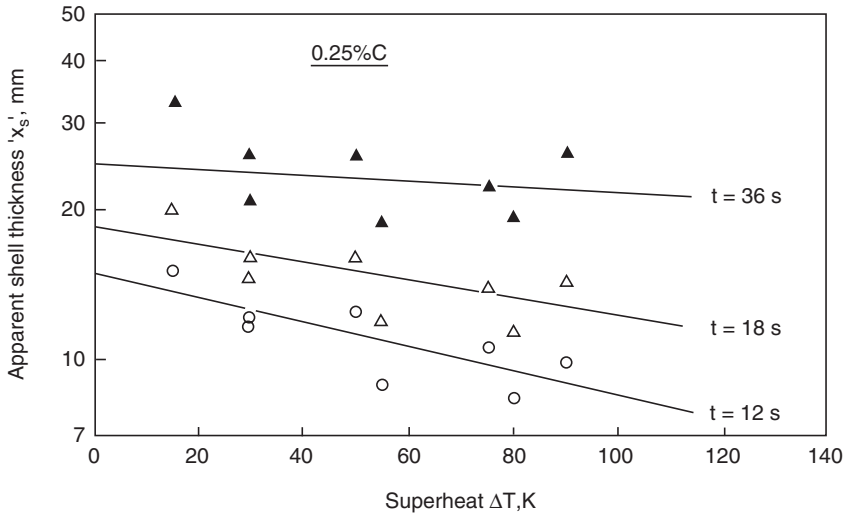

Fig. 4.35 Influence of superheat on shell thickness at various solidification times. *From Ref. 25.*

Several measures that influence the heat flow from the strand also influence the K-factor. Hence, K is expected

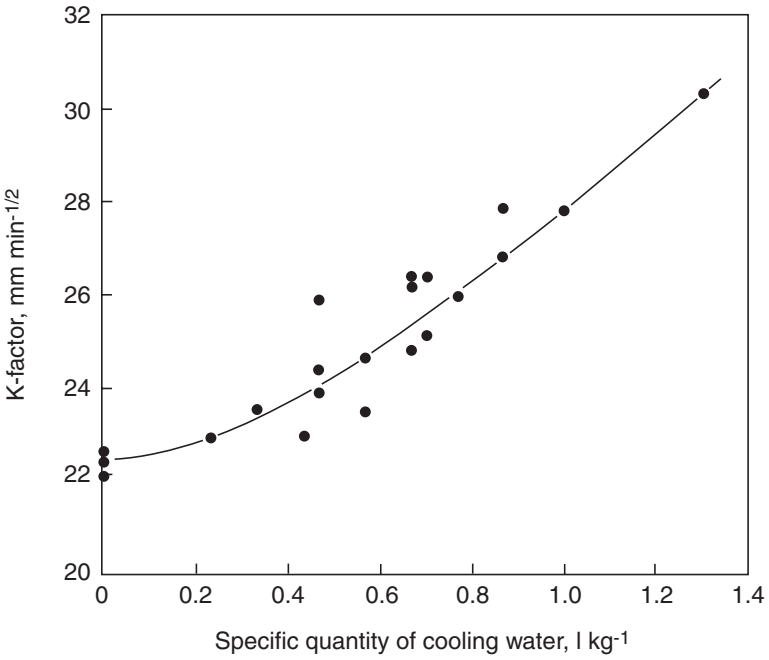

Fig. 4.36 Influence of the specific quantity of cooling water in the secondary cooling zone on the parabolic rate 'constant' K for Ck 25. *From Ref. 56.*

to be larger for open pouring with oil lubrication than for closed pouring with mold powder addition (see data on heat flux density in Fig. 4.15). In the list of K-values compiled by Wolf,[25] the K-values for oil lubrication range from 18.0 to 38.4 mm $min^{-0.5}$ (average of 24.6 mm $min^{-0.5}$ for seven values) and those for flux lubrication from 14.1 to 21.9 mm $min^{-0.5}$ (average of 17.9 mm $min^{-0.5}$ for 31 values), for steel with ≤ 0.15% C.

The extent of contact between the strand and the mold influences shell growth in a similar way as heat flux density. Hence, taper of the mold and guidance of the strand below the mold, along with the manner of strand shrinkage, have an effect, which has the maximum around 0.1% C. Systematic investigations of such effects, however, do not seem to be available.

K-factors for the secondary cooling zone increase with the amount of spray water. Experimental data obtained on billets with steel of 0.25% C (Ck 25) are shown in Fig. 4.36.

4.4.2 Relationship Between Shell Thickness and Heat Flux Density in the Mold

Although the shell thickness can readily be computed from the heat flux density at the strand surface by using a theoretical numerical model, simple approximate formulae are useful for fast estimates.

Such a formula can be obtained by equating the heat removed at the surface of the strand with the enthalpy loss of the strand:

$$\frac{1}{v_c}\int_0^z q(z)\,dz = x_s(z)\,\rho\left[\Delta H_f + c_p\overline{\Delta T(z)}\right] \qquad \text{(Eq. 4.66)}$$

from which follows:

$$x_s(z) = \frac{\int_0^z q(z)\,dz}{v_c\,\rho\left[\Delta H_f + c_p\overline{\Delta T(z)}\right]} \qquad \text{(Eq. 4.67)}$$

In the term $c_p\ \overline{\Delta T(z)}$, representing the loss of enthalpy of the solid shell, $\overline{\Delta T(z)}$ is an average decrease of temperature below T_f of the shell at the position z. Equation 4.67 has been used by Vogt and Wuennenberg[11] for the calculation of shell thickness at the end of the mold, with $\overline{\Delta T(L_m)}$ = 100°C finding good agreement with the measured shell thickness data.

Nevertheless, $\overline{\Delta T(z)}$ must not be assumed, but can be computed. Taking the temperature profile in the shell to be linear, $\overline{\Delta T(z)}$ is half of the temperature difference between the solidification front and the strand surface, $[T_f - T_0(z)]/2$. This temperature difference can be obtained from:

$$q(z) = \lambda \frac{T_f - T_0(z)}{x_s(z)} \qquad \text{(Eq. 4.68)}$$

Inserting equation 4.68 into 4.66 and solving for $x_s(z)$ yields:

$$x_s(z) = -\frac{\lambda\,\Delta H_f}{c_p\,q(z)} + \sqrt{\left(\frac{\lambda\,\Delta H_f}{c_p\,q(z)}\right)^2 + \frac{2\lambda}{\rho\,c_p\,v_c\,q(z)}\int_0^z q(z)\,dz} \qquad \text{(Eq. 4.69)}$$

The integral $\int_0^z q(z)\,dz$ can be computed numerically from the measured q(z) data, or analytically using an expression of the types given by equations 4.30 to 4.34.

It should be kept in mind that equation 4.69 is derived for pure iron solidifying with a planar solidification front and, consequently, it is applicable only for steels with low content of other elements solidifying with a short mushy zone.

4.4.3 Data for the Shell Thickness at the Exit of the Mold

A datum particularly important is the shell thickness $x_{s,m}$ at the exit of the mold because it gives a measure for the risk of breakouts. Fig. 4.37 shows values of $x_{s,m}$ reported in the literature as a function of strand velocity. The shell thickness decreases quite strongly with increasing strand velocity.

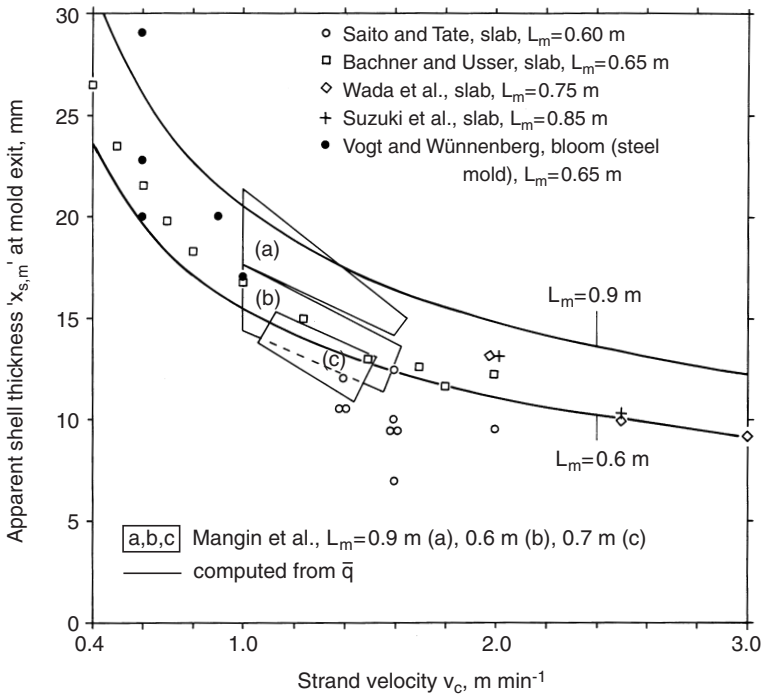

Fig. 4.37 Data on shell thickness at mold exit. The curves are computed with equations 4.73 and 4.74 using equation 4.46 for the average heat flux density $\bar{p}$. *From Refs. 11, 15, 20, 21, 53, 57.*

A number equation for $x_{s,m}$ as a function of average heat flux density $\bar{q}$ and of casting velocity v_c can be derived from equation 4.69 in the following manner. The local heat flux density $q(L_m)$ at the exit of the mold is set proportional to the average heat flux density $\bar{q}$:

$$q(L_m) = f_q\ \bar{q} = \frac{f_q}{L_m}\int_0^{L_m} q(z)\,dz \qquad \text{(Eq. 4.70)}$$

Hence, from equation 4.69 follows:

$$x_{s,m} = -\frac{\lambda\ \Delta H_f}{f_q\ c_p\ \bar{q}} + \sqrt{\left(\frac{\lambda\ \Delta H_f}{f_q\ c_p\ \bar{q}}\right)^2 + \frac{2\,\lambda\ L_m}{f_q\ c_p\ \rho\ v_c}} \qquad \text{(Eq. 4.71)}$$

For the normal q-z relationship with exponential decrease of q with z, the factor f_q can be computed with equations 4.28 and 4.38, that is:

$$f_q = \frac{q(L_m)}{\bar{q}} = \frac{\alpha\ L_m\ e^{-\alpha L_m}}{1 - e^{-\alpha L_m}} \qquad \text{(Eq. 4.72)}$$

Using ΔH_f = 262,000 J kg^{-1}, c_p = 750 J kg^{-1} K^{-1}, λ = 32 W K^{-1} m^{-1}, ρ = 7500 kg m^{-3} and f_q = 0.62 or 0.47 for L_m = 0.6 m or 0.9 m, respectively, yields:

$$x_{s.m} = -\frac{1803}{\bar{q}} + \sqrt{\left(\frac{1803}{\bar{q}}\right)^2 + \frac{661}{v_c}} \quad (\text{for } L_m = 0.6\text{ m}) \qquad \text{(Eq. 4.73)}$$

$$x_{s.m} = -\frac{2378}{\bar{q}} + \sqrt{\left(\frac{2378}{\bar{q}}\right)^2 + \frac{1307}{v_c}} \quad (\text{for } L_m = 0.9\text{ m}) \qquad \text{(Eq. 4.74)}$$

where $x_{s,m}$ is in mm, $\bar{q}$ in W cm^{-2}, L_m in m and v_c in m min^{-1}. The drawn curves in Fig. 4.37 are computed with equations 4.73 and 4.74 using equation 4.46 for $\bar{q}$.

4.5 Modeling

Mathematical modeling of heat transfer in continuous casting has been performed for many years. Initially, the objective was, as in other research areas, to achieve a better general understanding of the process, or certain phenomena in the process. Later, modeling was used for optimizing cooling strategies in real casting practice or in the design of casting machines. Recently, mathematical modeling is applied for direct control of the casting process. That is, the temperature field of the strand is computed on-line during casting and is used for adjustment of water sprays in the case of disturbances. There are many interesting possibilities to connect on-line thermal tracking of the strand with experience or with mathematical models on defect formation, and to build quality control systems around the thermal model.

The heat flow equation applicable to continuous casting with rectangular strand cross-section is:

$$\rho\left(\frac{\partial H}{\partial t} + v_c\frac{\partial H}{\partial z}\right) = \frac{\partial}{\partial x}\left(\lambda\frac{\partial T}{\partial x}\right) + \frac{\partial}{\partial y}\left(\lambda\frac{\partial T}{\partial y}\right) + \frac{\partial}{\partial z}\left(\lambda\frac{\partial T}{\partial z}\right) \qquad \text{(Eq. 4.75)}$$

where $v_c = v_z$ (constant in the z-direction) is the rate of strand movement. The origin of the z-coordinate is at the meniscus. At steady state, which is the normal casting operation, equation 4.75 reduces to:

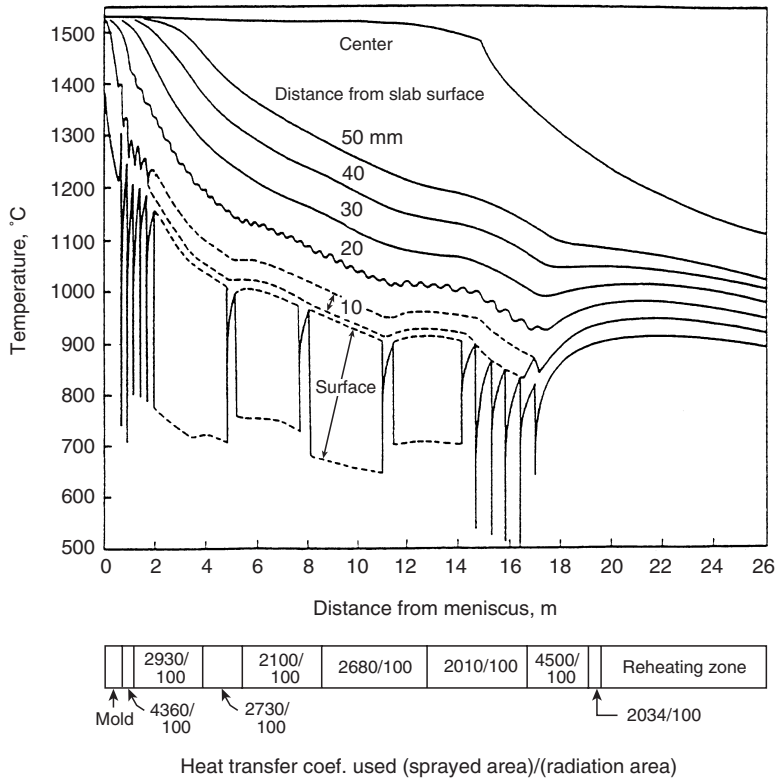

Fig. 4.38 Example for modeling of temperature field in a continuously cast slab. *From Ref. 50.*

$$\rho\, v_c \frac{\partial H}{\partial z} = \frac{\partial}{\partial x}\left(\lambda \frac{\partial T}{\partial x}\right) + \frac{\partial}{\partial y}\left(\lambda \frac{\partial T}{\partial y}\right) + \frac{\partial}{\partial z}\left(\lambda \frac{\partial T}{\partial z}\right) \qquad \text{(Eq. 4.76)}$$

which is solved with the appropriate boundary condition at the surface x = 0 and taking the center as a symmetry plane. At the broad side of slabs, and also at the sides of billets and blooms as long as the shell is still sufficiently thin (and if the cooling at the surface is uniform in lateral direction), the term $\partial\lambda(\partial T/\partial y)/\partial y$ for conduction in the lateral direction can be omitted. Usually, the conductive term $\partial\lambda(\partial T/\partial z)/\partial z$ is also neglected because the transport of enthalpy in the z-direction by conduction is much smaller (in the average) than by convection. Hence, the simplest form of the heat flow equation used for modeling of heat transfer in continuous casting is:

$$\rho\, v_c \frac{\partial H}{\partial z} = \frac{\partial}{\partial x}\left(\lambda \frac{\partial T}{\partial x}\right) \qquad \text{(Eq. 4.77)}$$

However, the omission of $\partial\lambda(\partial T/\partial z)/\partial z$ is not permissible if the temperature fluctuations at the surface in the secondary cooling zone due to the roll contact and water impingement are to be computed. These fluctuations can be as large as several hundred degrees, causing steep z-gradients of temperature, which have to be taken into account in the proper heat flow analysis (see Section 4.3.3).

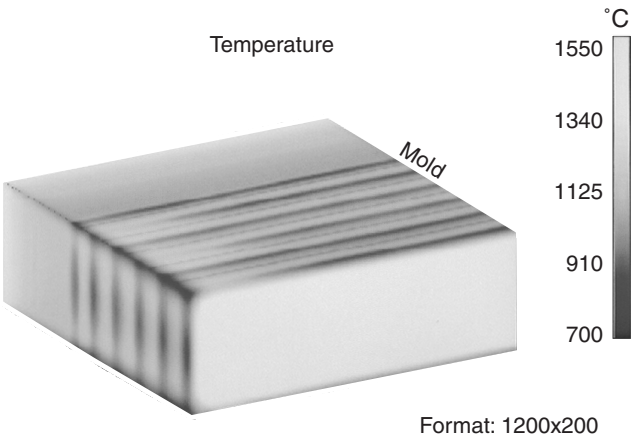

Fig. 4.39 Computed surface temperature field of a slab in the mold and the first part of the secondary cooling zone (three-dimensional model). *From Ref. 58.*

The enthalpy curve H(T) of the steel depends on the phase diagram, which again depends on the steel composition. Also, density and thermal conductivity depend on temperature and composition. Hence, additional software is needed to obtain the material data. In fact, more work is contained in the development of good material data algorithms than in setting up the actual solution procedure for the heat flow equation.

Fig. 4.38 shows an example for a heat flow analysis.[50] Cooling in the secondary cooling zone was with flat spray nozzles, and it was assumed that solely radiation occurred beyond the narrow spray areas. The computed temperature dips at the surface in the impinged zones are partially as low as 500°C, the effect being strongest in the region below the mold. However, at about 20 mm depth from the surface, the fluctuations have almost become dampened out. The fraction of the sprayed area of the roll spacing was less than 10% in this case. Of course, the dips decrease if the water is distributed more uniformly. Another example is given in Fig. 4.39.[59] Here, the surface temperature of the upper part of the strand is demonstrated by a computed 'real' color picture. The three-dimensional model was used, taking the heat transfer coefficient at the edges, about half of those at the sides.

4.5.1 Thermal Tracking

Although first computations of temperature profiles and shell thickness can be performed using the relationships for heat flux density and heat transfer coefficients given in Sections 4.2 and 4.3, for real on-line control such a procedure is not sufficiently accurate and the exact boundary conditions must be deduced from the surface temperature measurements performed at the specific casting machine. Further, the computations must be sufficiently fast, and the model must be non-stationary. Various models for real-time simulation have been described recently.[59–62]

In the work reported by Spitzer et al.,[59] the heat transfer coefficient in the various cooling zones were expressed by equations of the form:

$$h_i = a_i + b_i\xi + c_i\xi^2 \qquad \text{(Eq. 4.78)}$$

or

$$h_i = a_i + b_i\xi c_i \qquad \text{(Eq. 4.79)}$$

with the index i referring to the cooling zone i. ξ is a variable that can represent different types of process parameters depending on whether it is for the mold or a spray cooling zone. The parameters a_i, b_i and c_i are determined by tracking strand slices on their way through the caster, and by minimizing the differences between measured and computed temperatures with a least squares method, in order to give optimum agreement with surface temperatures obtained with pyrometers

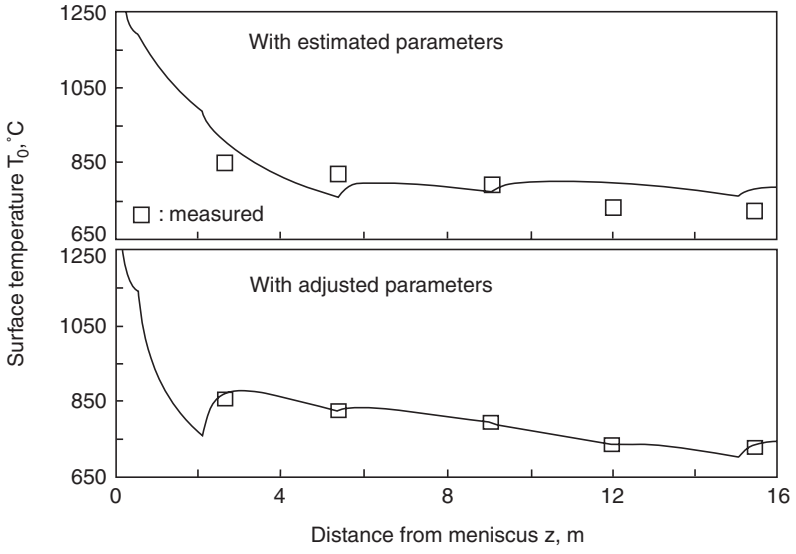

Fig. 4.40 Model adjustment to measured surface temperatures along the strand in the secondary cooling zone. *From Ref. 59.*

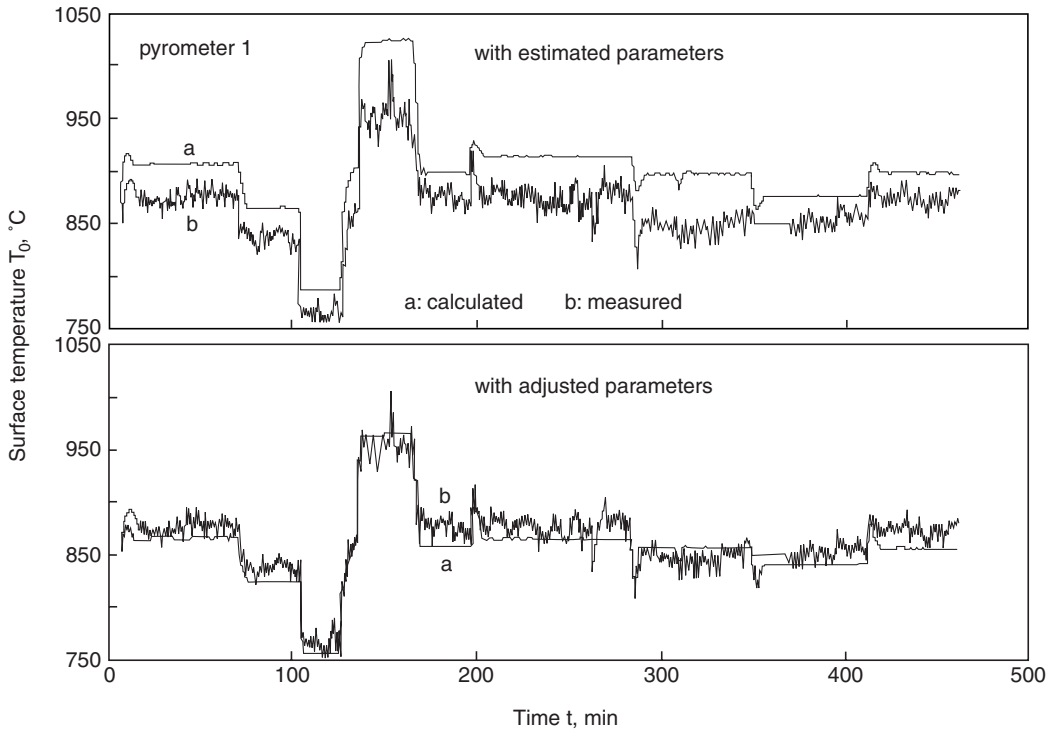

Fig. 4.41 Comparison of measured and calculated surface temperature as a function of time (position of the first thermocouple in Fig. 4.40). *From Ref. 59.*

along the strand. For instance, if there are n cooling zones and all three coefficients are used, 3n coefficients have to be determined. If the temperature is measured at k positions along the strand, and if l slices are selected covering different casting conditions, kl temperature differences are minimized to find 3n coefficients.

The procedure has been described for a caster with six cooling zones (mold plus five secondary cooling zones).[59] Five pyrometers were installed, and seven strand slices were tracked. ξ is the casting speed for the mold, and for the secondary zones it is the spray water density. The effect reached by the adjustment is seen in Figs. 4.40 and 4.41. Fig. 4.40 shows the surface temperatures as a function of distance from the meniscus, with both the estimated and adjusted coefficients. The measured temperature values are given by the symbols. The results shown in this figure are for a typical steady state casting condition. In Fig. 4.41, for the first pyrometer position (uppermost pyrometer) the calculated temperatures are given as a function of the time after start of casting and are compared to measured temperatures. Again, the results obtained with both the estimated and the adjusted coefficients are given. Within the observed period, casting speed and spray water densities were varied. It can be concluded from these results and others that, by adjustment of boundary conditions on the basis of specifically devised temperature measurements, an agreement between the real and computed surface temperatures can be attained of mostly ± 20°C or better.

4.5.2 Quality Control Systems

It has already been mentioned that thermal tracking is the basis of a quality control system. For the conclusion of this chapter, a proposal for such a system[62] is shown in Fig. 4.42. The heart of the system is the thermal model. The auxiliary software for the thermal model comprises the algorithms (right side) for the computation of the phase diagram, enthalpy, thermal conductivity, density and other material properties and the algorithm (left side) for the optimization of the boundary conditions. The lower field at the right shows the quality control tools. The defects are divided into

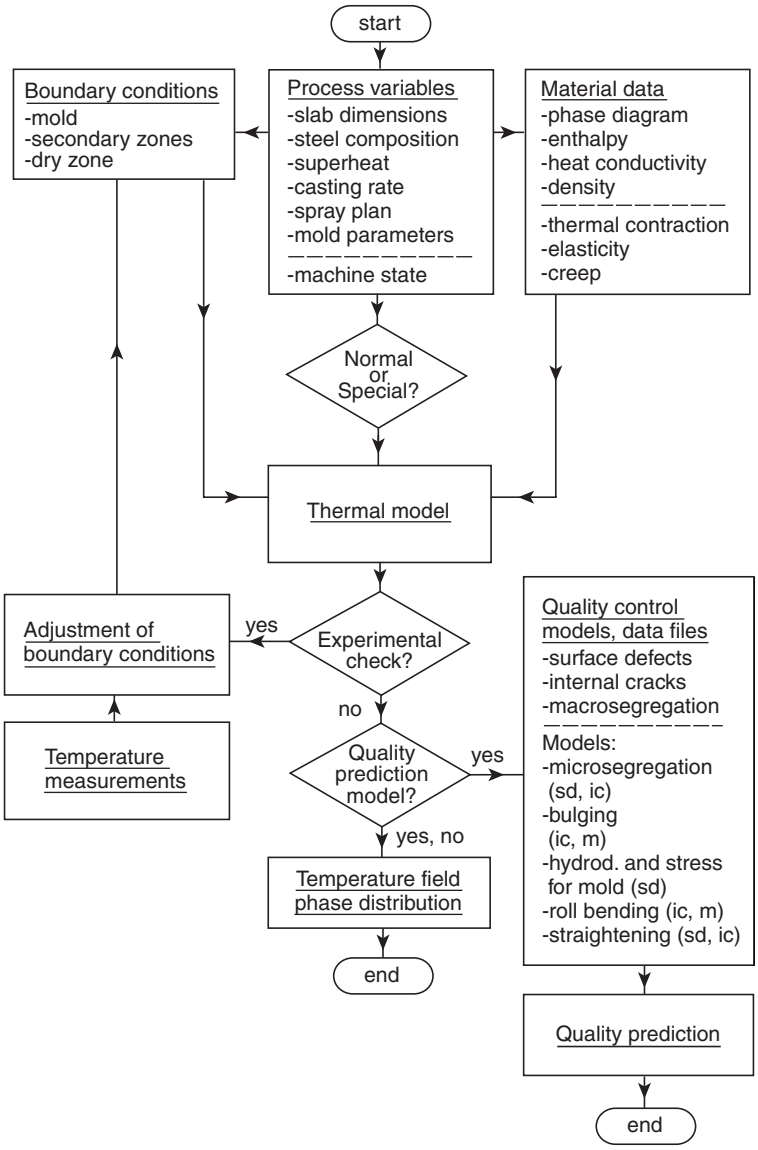

Fig. 4.42 Quality control system for continuous casting of slabs. *From Ref. 62.*

three classes: surface defects, internal cracks and macrosegregation. The predictions are made on the basis of mathematical models and empirical data files. Non-normal events are stored (e.g., excessive bulging values[62]), and the respective parts of the strand are later subjected to a quality inspection.

References

1. M.S. Jenkins, *Proc. Steelmaking Conf.*, 78 (1995), Nashville, Tenn., Iron and Steel Society, pp. 315–320.
2. S. Ohmiya, K.-H. Tacke and K. Schwerdtfeger, *Ironmaking and Steelmaking*, 10 (1983), pp. 24–30.
3. J.-F. Holzhauser, K.-H. Spitzer and K. Schwerdtfeger, *Steel Research*, 70 (1999), No. 7, pp. 252–258.

4. J.-F. Holzhauser, K.-H. Spitzer and K. Schwerdtfeger, *The influence of casting aids on the heat transfer in the mold, the surface quality and incidence of breakouts in the continuous casting of steel*, ECSC Contract 7210 CA/139 (1990), Final Report EUR 12198 DE.
5. R. Alberny, *Int. Symp. Casting and Solidification of Steel* (1/1977), Luxemburg, IPC Science Technol. Press, Guildford, EUR, 5903 d, e, f.
6. R.B. Bird, W.E. Stewart and E.N. Lightfoot, *Transport Phenomena* (1966), John Wiley & Sons, New York.
7. K. Wilde, *Waerme- und Stoffuebergang in Stroemungen* (1978), Steinkopf.
8. E. Schmidt, *Properties of Water and Steam in SI-Units* (1969), Springer.
9. N.A. Lange, *Handbook of Chemistry* (1961), McGraw-Hill, New York.
10. K. Schwerdtfeger, "Erstarrung metallischer Schmelzen," edited by P.R. Sahm (1988), DGM Informationsgesellschaft, pp. 205–224.
11. G. Vogt and K. Wuennenberg, *Klepzig Fachberichte*, 80 (1972), pp. 491–494.
12. H.L. Gilles, *Proc. Steelmaking Conf.* (1993), Iron and Steel Society, pp. 315–329.
13. J. Savage and W.H. Pritchard, *J. Iron and Steel Inst.*, 178 (Nov. 1954), pp. 269–277.
14. D.P. Evteev, *Stahl in English*, 8 (Aug. 1969), pp. 708–711.
15. M. Suzuki, S. Miyahara, T. Kitagawa, S. Uchida, T. Mori and K. Okimoto, *Tetsu-to-Hagané*, 78 (1992), pp. 113–120.
16. R. Alberny, A. Leclercq, D. Amaury and M. Lakousse, *Rev. Métallurgie* (1976), No. 7–8, pp. 545–557.
17. A. Leclercq, *Coulée et solidification de l'acier*, Tome II, IRSID, Com. Communantés Européennes No. 6210-50, Rapport Final (1979), EUR 6216 II FR.
18. J. Dubendorff, J. Sardemann and K. Wuennenberg, *Stahl und Eisen*, 103 (1983), No. 25–26, pp. 1327–1332.
19. U. Horbach, J. Kockentiedt and W. Jung, *Stahl und Eisen*, 117 (1997), No. 12, pp. 95–101.
20. E. Bachner and M. Ussar, *Stahl and Eisen*, 96 (1976), No. 5, pp. 185–190.
21. M. Mangin, M. Nicolas, J. Foussal, J.F. Marioton, M. Larrecq and M. Wanin, *Rev. Métallurgie*, CIT (Fev. 1985), pp. 111–118.
22. M.J. Mundin, J.L.R. Pimenta, C.A.G. Valadares and P.F. Pereira, *Proc. Int. Conf. Continuous Casting* (1985), London, paper 50.1–50.6.
23. G. Backmann, A. Koethe, W. Loeser, J. Richter, T. Schubert, S. Thiem and L. Hering, *Stahl und Eisen*, 113 (1993), No. 2, pp. 63–66.
24. J.E. Lait, J.K. Brimacombe and F. Weinberg, *Ironmaking and Steelmaking* (Quarterly) (1974), No. 2, pp. 90–97.
25. M. Wolf, *Ueber Legierungseinfluesse auf Waermeabfuhr und Schalenwachstum in der Kokille bei der Erstarrung von Stahlstrangguss* (1978), Thesis, École Polytechnique Fédérale de Lausanne.
26. L. Hering and H.-W. Fenzke, *Stahl und Eisen*, 112 (1992), No. 7, pp. 91–95.
27. S.N. Singh and K.E. Blazek, *J. Metals* (Oct. 1974), pp. 17–24.
28. K.E. Blazek, *Iron and Steelmaker* (Oct. 1987), pp. 36–38.
29. R. Bruder, J. Wolf and A. Borowski, pp. 301–304.
30. H. Abratis, F. Hoefer, M. Juenemann, J. Sardemann and H. Stoffel, *Stahl und Eisen*, 116 (1996), No. 9, pp. 73–78.
31. M.C. Boichenko, *Continuous Casting of Steel* (1961), Butterworth.
32. E. Mizikar, *Iron and Steel Engineer*, 47 (June 1970), pp. 53–60.
33. J.K. Brimacombe, P.K. Agarwal, L.A. Baptista, S. Hibbins and B. Prabhakar, *Steelmaking Proc.*, 63 (1980), pp. 235–252.
34. M. Mitsutsuka, *Tetsu-to-Hagané*, 69 (1983), No. 2, pp. 268–274.
35. U. Reiners, *Waermeuebertragung durch Spritzwasserkuehlung heisser Oberflaechen im Bereich der stabilen Filmverdampfung* (1987), Dr.-Ing. Dissertation, Technische Universitaet Clausthal.
36. K. Sasaki, Y. Sugitani and M. Kawasaki, *Tesu-to-Hagané*, 65 (1979), No. 1, pp. 90–96.
37. H. Jacobi, G. Kaestle and K. Wuennenberg, *Ironmaking and Steelmaking*, 11 (1984), No. 3, pp. 132–145.

38. H. Mueller and R. Jeschar, *Archiv Eisenhuettenwesen*, 44 (1973), pp. 589–594.
39. L. Bolle and J.C. Moureau, *Int. Conf. Heat Mass Transfer Metallurgical Processes* (1979), Dubrovnik, pp. 527–534.
40. A. Etienne and B. Mairy, *C.R.M*., 55 (1979), pp. 3–13.
41. C.J. Hoogendorn and R. den Hond, *5th Int. Heat Transfer Conf. IV* (1974), Tokyo, Paper B 3.12, pp. 135–138.
42. M. Shimada, N. Takeda and S. Akabane, *Tesu-to-Hagané*, 62 (1976), pp. 372–379.
43. P. Benoit, M. Rouzier, A. Perroy and J. Petegnief, *Rev. Métallurgie*, 75 (1978), pp. 363–373.
44. M. Mitsutsuka and K. Fukuda, *Trans*. *ISIJ,* 21 (1981), pp. 689–698.
45. T. Murakami, T. Sampei, K. Tezuka, F. Hazumi and H. Goukon, *Trans*. *ISIJ,* 25 (1985), B 339.
46. R. Gardon and J. Cobonpue, "Intern. Develop. in Heat Transfer," *Proc. 2nd Int. Heat Transf. Conf*. (1962), ASME, pp. 454–460.
47. P.M. Bridlik and V.K. Savin, *Inzhenerno-Fizicheskii Zhurnal*, 8 (1965), No. 6, pp. 146–155, English translation, pp. 91–98.
48. B. Barber, B. Patrick, P. Watson, R. York, F. Kitching, H. Sha, K. Kraushaar and K.-H. Spitzer, *Revue de Métallurgie*, ATS-JS (1996), pp. 148–149.
49. M. Wolf, *Ironmaking and Steelmaking*, 13 (1986), No. 5, pp. 248–257.
50. K. Kawakami, T. Kitagawa, K. Murakami, Y. Miyashita, Y. Tsuchida and T. Kawawa, *Nippon Kokan Technical Report Overseas* (1982), No. 36, pp. 26–41.
51. J.E. Lait, J.K. Brimacombe and F. Weinberg, *Ironmaking and Steelmaking* (Quarterly) (1974), No. 1, pp. 35–42.
52. J.E. Lait, J.K. Brimacombe, F. Weinberg and F.C. Muttitt, *Proc. 56th National Open Hearth and Basic Oxygen Steel Conf*. (1973), Cleveland, pp. 269–302.
53. T. Wada, M. Suzuki and T. Mori, *Iron and Steelmaker*, 14 (1987), No. 9, pp. 31–38.
54. G. Tarmann and G. Forstner, *Radex Rundschau* (1966), No. 1, pp. 51–58.
55. J. Chipman and C.R. FonDersmith, *Amer. Inst. Min. Met. Engrs. Tech. Publ*., No. 812, pp. 370–377.
56. W. Holzgruber and B. Tarmann, *Steel Times* (Aug. 1967), pp. 217–225.
57. K. Saito and M. Tate, *Proc. 56th National Open Hearth and Basic Oxygen Steel Conf*. (1973), Cleveland, pp. 238–267.
58. K.-H. Spitzer and K. Schwerdtfeger, unpublished research.
59. K.-H. Spitzer, K. Harste, B. Weber, P. Monheim and K. Schwerdtfeger, *ISIJ International*, 32 (1992), No. 2, pp. 848–856.
60. S. Loubenkilpi, E. Laitinen and R. Nieminen, *Met. Trans B,* 24B (1993), pp. 685–693.
61. K. Moerwald, K. Dittenberger and K.D. Ives, *Iron and Steelmaker*, 25 (1998), No. 4, 323–327.
62. K. Schwerdtfeger, *Proc. of Int. Conf. Computer-Assisted Materials Design and Process Simulation* (1993), Tokyo, pp. 1–10.

